Journal of Materials Chemistry A

ROYAL SOCIETY OF CHEMISTRY

REVIEW

View Article Online
View Journal

Cite this: DOI: 10.1039/d5ta03108g

Recent advances of photothermal technology in CO_2 capture and methanation

Yu Zhu, [a] Qiao Peng,[a] Muhammad Adnan Zeb,[a] Jinlong Zhang, [a] Juying Lei [b] and Lingzhi Wang *[a]

Received 20th April 2025
Accepted 13th August 2025

DOI: 10.1039/d5ta03108g

rsc.li/materials-a

Producing synthetic natural gas (SNG) from hydrogen *via* water electrolysis and industrial CO_2 addresses renewable energy surplus while integrating CH_4 into existing natural gas grids. However, the energy-intensive processes of hydrogen production, CO_2 capture, and methanation increase energy demands and emissions. Limited research focuses on cost reductions from a CO_2 perspective. Emerging photothermal technology shows promise in enhancing efficiency and reducing energy use in CO_2 capture and methanation. This review highlights advancements in photothermal materials design, cyclic CO_2 capture performance, catalysts, and the integration of capture and methanation. It also examines reactor designs and techno-economic assessments, concluding with challenges and future directions for practical application.

1. Introduction

Excessive reliance on fossil fuels results in substantial CO_2 emissions, contributing significantly to climate and environmental challenges.[1,2] Renewable energy sources, such as wind, solar, biomass, *etc.*, can lower CO_2 emissions at the source by replacing fossil fuels.[3,4] However, a large-scale, long-term plan is required to store excess power because renewable energy output is weather-dependent and intermittent.[5] Power-to-gas (PtG) systems offer a promising solution, allowing excess renewable electricity to be stored by converting it into hydrogen (H_2) and combining it with industrial CO_2 to produce synthetic natural gas (SNG).[6] This SNG is carbon-neutral and can be seamlessly integrated into existing infrastructure, providing a stable energy supply for power plants or the gas industry. The cost of large-scale SNG production is still high, despite the promising future. Few studies have examined ways to lower the cost of CO_2, whereas the majority of study has concentrated on lowering the cost of H_2.[7,8]

The cost of CO_2 in the SNG process is primarily made up of two processes: CO_2 capture and CO_2 methanation. By lowering the costs of these two processes, the overall cost of CO_2 can be decreased. Regarding CO_2 capture, the most advanced technology involves the chemical absorption method, with amine solvents serving as commonly used absorbers. Among them, physical adsorbents such as zeolite and carbon-based materials can adsorb CO_2 at low temperatures, while chemical adsorbents such as hydrotalcite and alkali calcium oxide can adsorb CO_2 at high temperatures.[9] However, recycling CO_2 with these methods typically requires high temperatures, leading to substantial energy consumption. A sustainable alternative is using solar energy to replace this energy-intensive process. Currently, solar-driven CO_2 recycling depends on two primary mechanisms. The first employs an innovative photo-responsive switch based on the steric-hindrance effect to regulate CO_2 adsorption and desorption. For example, azophenyl, a photo-responsive group, transitions from a *trans*- to *cis*-form under UV light, facilitating CO_2 release by spatially blocking the interaction between amine and CO_2 (Fig. 1a).[10,11] However, this method is usually limited by low CO_2 adsorption and desorption efficiency. The second mechanism utilizes a thermal response switch based on the photothermal effect to control

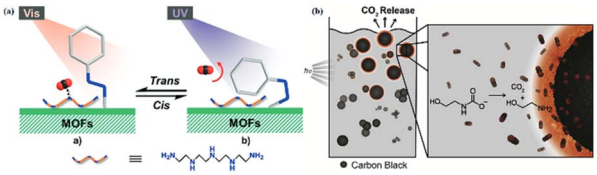

Fig. 1 (a) Tailorable CO_2 capture on the photo-responsive MOFs through an interaction between active sites and photo-responsive molecules. Reproduced with permission from ref. 10. Copyright 2019 *Angew. Chem. Int. Ed.* (b) Decarboxylation of MEA using the photothermal effect of CB nanoparticles. Reproduced with permission from ref. 12. Copyright 2016 *Carbon*.

[a]*State Key Laboratory of Green Chemical Engineering and Industrial Catalysis, Key Lab for Advanced Materials and Joint International Research Laboratory of Precision Chemistry and Molecular Engineering, Feringa Nobel Prize Scientist Joint Research Center, Institute of Fine Chemicals, School of Chemistry and Molecular Engineering, East China University of Science & Technology, Shanghai, 200237, China. E-mail: wlz@ecust.edu.cn*

[b]*Shanghai Engineering Research Center for Multi-Media Environmental Catalysis and Resource Utilization, East China University of Science & Technology, Shanghai, 200237, China*

CO_2 adsorption and desorption. For example, modified carbon black nanoparticles (CB NPs) have been used to facilitate the breakage of the chemical bond between CO_2 and the amine solvent through localized thermal effects of the photothermal mechanism, facilitating CO_2 release (Fig. 1b).[12] CO_2 recycling methods leveraging photothermal effects have garnered attention due to their high CO_2 recycling capacity, lower regeneration temperatures for adsorption and desorption, and the utilization of green energy inputs.

For CO_2 methanation, its catalytic methods include thermal catalysis,[13] electrocatalysis,[14] photocatalysis,[15] photoelectrocatalysis,[16] and photothermal catalysis.[17] Thermal catalysis often requires high temperature and high pressure. Electrocatalysis, while promising, struggles with energy efficiency due to the high overpotential required and the limited solubility of CO_2 in aqueous electrolytes, which restricts the current densities needed for economic viability.[18] Photocatalysis, powered by solar energy, offers energy input advantages over both electrocatalysis and thermal catalysis; however, its large-scale application is limited by challenges such as poor sunlight utilization, limited photocatalyst activity, and low product selectivity.[19] Photothermal catalysis emerges as a promising alternative by combining light and heat to drive reactions.[20] This approach overcomes the limitations of low conversion and selectivity in photocatalysis while also mitigating the energy demands and catalyst deactivation issues encountered in thermal catalysis. Despite its advantages, large-scale photothermal methanation faces challenges in designing catalysts that achieve high selectivity, efficiency, and stability.[20] A deeper understanding of the roles of light and heat in photothermal catalytic methanation is essential to advance catalyst design and enhance reaction performance.

Reducing the cost of CO_2 capture and methanation in SNG production necessitates a focused and strategic approach to CO_2 utilization. Current researches predominantly target CO_2 capture and methanation as separate processes, with growing interest in integrating the two. Although the integration of photothermal CO_2 capture and methanation is still in its early stages, its significant economic potential positions it as a compelling area for further investigation. Several existing reviews have systematically summarized the catalyst design, performance evaluation, and reaction mechanisms related to photothermal CO_2 methanation.[21–23] However, these studies primarily focus on catalytic systems, and few have approached the topic from a system-level perspective that integrates CO_2 capture and conversion. In particular, no comprehensive review has yet addressed the emerging role of photothermal technology in enabling a seamless CO_2 capture-to-utilization pathway. In this review, we take a CO_2-centered perspective to evaluate the applicability of photothermal technology in enhancing both CO_2 capture and regeneration. We summarize recent advances in photothermal CO_2 methanation photocatalysts and further explore the feasibility and progress of coupling photothermal CO_2 capture with methanation. To our knowledge, this is the first review that provides an integrated analysis of photothermal systems from the viewpoint of capture-to-conversion integration. We also assess practical and economic considerations by analyzing reactor designs and conducting techno-economic evaluations of the integrated process. Finally, based on the current state of the field, we identify key scientific and engineering challenges and propose future directions for advancing photothermal technologies for CO_2 capture and methanation.

2. Photothermal mechanisms

To optimize photothermal performance, ideal materials must exhibit strong absorption in the visible and near-infrared regions, which together account for approximately 95% of solar energy. Typical examples include precious metals,[24] defective semiconductors,[25] carbon nanomaterials,[12] and some organic polymers.[26] These materials generate charge carriers through electronic transitions after absorbing photons. If electrons and holes recombine, they emit fluorescence; if the absorbed photon energy is released as heat through non-radiative relaxation, it produces a photothermal effect.[27] The photothermal effect can be classified by the type of relaxation mechanism: (1) non-collisional relaxation within molecules, where excited electron energy redistributes through coupling with various vibrational modes (Fig. 2a); (2) collisional vibrational relaxation among molecules and within crystal lattices, where energy from charge carriers is converted into heat through intermolecular and atomic collisions, distributing thermal energy throughout the system (Fig. 2b).[28]

Photothermal materials can be categorized based on their light absorption properties: (1) transition metal-based photothermal materials, primarily including coinage metals (*e.g.*, Au, Ag) and Group VIII metals (*e.g.*, Ni, Co, Pt). Coinage metals exhibit strong localized surface plasmon resonance (LSPR) in the visible to near-infrared region, leading to the generation of enhanced electromagnetic fields and localized surface hotspots. In contrast, group VIII metals typically display weaker LSPR responses but are widely employed in photothermal catalysis

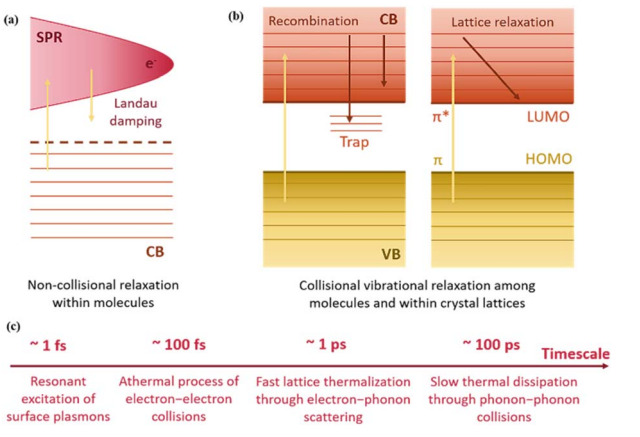

Fig. 2 Two type of relaxation mechanism of the photothermal effect. (a) Non-collisional relaxation within molecules. (b) Collisional vibrational relaxation among molecules and within crystal lattices. (c) A series of energy conversions and redistributions about the photothermal effect.

due to their excellent catalytic properties and broad light absorption capabilities. (2) Broad-spectrum absorbers, such as defective semiconductors, carbon nanotubes, graphene, and polypyrrole, which enhance photothermal conversion by extending photon absorption across visible and near-infrared regions.[29,30] To streamline the discussion in this review, we categorize photothermal materials into two representative groups (Fig. 3): transition metal-based and non-metallic photothermal materials.

The photothermal effect involves a series of energy conversions and redistributions. In noble metals, the specific process of photothermal effects based on LSPR is as follows: (1) resonant excitation of surface plasmons, generating a large number of photogenerated hot electrons through Landau damping (~1 fs); (2) an athermal phase characterized by electron–electron collisions (~100 fs); (3) rapid lattice thermalization facilitated by electron–phonon scattering (~1 ps); and (4) gradual thermal dissipation through phonon–phonon collisions, distributing the heat throughout the entire crystal (~100 ps) (Fig. 2c).[28,31] All these processes occur within the femtosecond to picosecond time range. Similar to noble metals, non-metallic materials like semiconductors and carbon nanotubes primarily convert light energy into thermal energy through vibrational processes. As mentioned earlier, the main difference lies in the fact that noble metals enhance the efficiency of photon absorption by resonating with specific frequencies, while non-metallic materials achieve improved photon utilization by broadening the absorption spectrum.[32] Additionally, due to the lower electron mobility in non-metallic materials, electrons and holes are prone to recombination, resulting in radiative emissions such as fluorescence or phosphorescence. This luminescence competes with the photothermal effect, as radiative re-emission reduces thermal conversion efficiency. To optimize light-to-heat conversion, it is essential to minimize radiative emission, for example, by enhancing the stacking of conjugated or layered materials, which helps suppress luminescence and improve photothermal efficiency.[28]

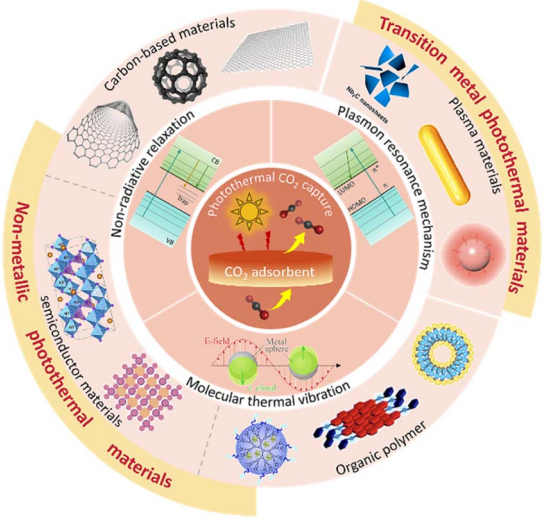

Fig. 3 Overview of the mechanisms and categories of photothermal materials.

3. Photothermal technology for cyclic CO_2 capture

Photothermal CO_2 capture leverages a cyclic process of CO_2 adsorption and desorption driven by the self-heating effect from solar energy. Effective materials for this process should possess both high CO_2 capture capacity and strong photothermal conversion ability, typically achieved by combining a CO_2 adsorbent with a photothermal agent.[33] Commonly used adsorbents include porous nanomaterials like metal–organic frameworks (MOFs) and polymers like polyethylenimine (PEI), which contain amine groups that react with CO_2 to form carbamate *via* single C–N bonds. Photothermal agents aid in desorption by providing the energy required to break these bonds.

For transition metals, Ag and Au are the most commonly employed. Using Ag/UiO-66 composites synthesized through a one-pot solvent-thermal reaction as a demonstration,[34] UiO-66 MOF, with a periodic porous structure and high stability, serves as the CO_2 adsorbent due to its microporous skeleton structure and high surface areas, and the supported Ag nanocrystals (Ag NCs) was used as the photothermal agent for converting light energy into local heat energy under visible light irradiation.[29] The heating effect enables the release of CO_2 adsorbed in MOF, and its desorption capacity can be adjusted by controlling the Ag content and light intensity. Under the 400–500 nm visible-light irradiation with an intensity of 0.94 W cm^{-2}, the Ag/UiO-66-3 composite with the highest Ag content showed the highest gas release capacity (Fig. 4a). Similarly, Sun *et al.* prepared

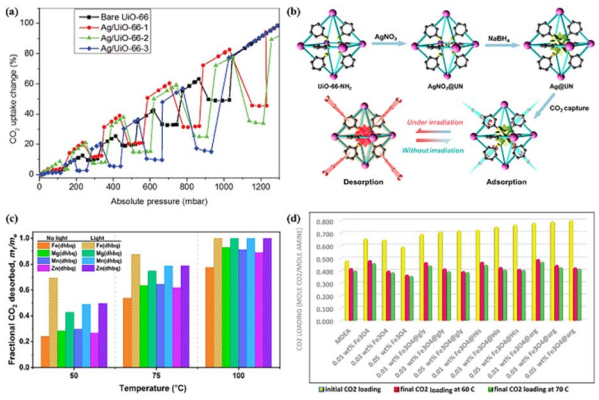

Fig. 4 (a) Photo-switching of normalized CO_2 uptakes and release of catalysts by periodically exposing them. Reproduced with permission from ref. 34. Copyright 2016 *Advanced Functional Materials*. (b) The synthesis of Ag@UN. Reproduced with permission from ref. 35. Copyright 2023 *Separation and Purification Technology*. (c) Bar chart showing the fractional degree of CO_2 desorption in M(dhbq) CPs at different conditions. Reproduced with permission from ref. 36. Copyright 2023 *ChemRxiv*. (d) Effect of different nanofluids on the final CO_2 loading at the end of 72 min regeneration process with different temperature. Reproduced with permission from ref. 33. Copyright 2023 *Separation and Purification Technology*.

Ag@UN composites by *in situ* reduction of Ag NPs in UiO-66-NH_2.[35] Compared to UiO-66, UiO-66-NH_2 exhibits enhanced visible light absorption and an increased alkaline group content, facilitating CO_2 adsorption and light-induced desorption. Under light irradiation, Ag NPs convert light into heat *via* the photothermal effect, precisely heating the active sites (Fig. 4b). The optimized Ag@UN sample achieved nearly 100% CO_2 desorption at 370 and 580 mmHg under light exposure in isothermal tests at room temperature, whereas the original UiO-66-NH_2 desorbed only 22.5% of CO_2 at 600 mmHg. In addition, dielectric materials with visible light absorption capability can also serve as photothermal agents for promoting cyclic CO_2 capture. For examples, Cheung's group reported four MOFs, M(dhbq)$(H_2O)_2$ with visible light response (where dhbq = 2,5-dihydroxy-1,4-benzoquinone, M = Fe, Mg, Mn or Zn).[36] Among them, Fe(dhbq) showed the strongest light absorption ability, the highest working capacity and excellent cyclic adsorption stability. Under visible light irradiation (1000 W m^{-2}, 10 min, 100 kPa), the CO_2 released by Fe(dhbq) was as high as 47.6%, which was equivalent to 37.5 g kg^{-1} working capacity (Fig. 4c). Additionally, black dielectric materials such as Fe_3O_4, known for their wide absorption in the visible spectrum, are frequently employed as photothermal agents. For example, Keshavarz's group modified the surface of Fe_3O_4 magnetic NPs with various amino acid groups, such as arginine, histidine, and glycine, using a wet dipping method.[33] CO_2 adsorption and desorption experiments using a nanofluid composed of these modified NPs in varying concentrations with 10% methyldiethanolamine revealed that Fe_3O_4 NPs possess excellent thermal properties, significantly enhancing the heat transfer rate of the nanofluid. Moreover, surface modification with amines improved both CO_2 capture efficiency and the hydrophilicity of the nanoparticles (Fig. 4d).

Carbon-based materials are also commonly used photothermal conversion agents.[40] For instance, Wang's group developed porous particles composed of polylactic acid and polyethylenimine (PLA–PEI), incorporating carbon nanotubes (CNTs) with photothermal conversion capabilities into the particle matrix.[37] These porous PLA–PEI particles could effectively regulate the adsorption and desorption of CO_2 by varying the light intensity. This light-driven adsorption–desorption process is stable over 10 cycles at room temperature (Fig. 5a). However, during the CO_2 desorption, most systems require temperatures above 90 °C to achieve complete CO_2 desorption, which can lead to solvent evaporation and is difficult to achieve under natural light conditions. Two strategies can mitigate these challenges: (1) employing non-liquid phase CO_2 adsorbents and (2) reducing the CO_2 desorption temperature to make the process more energy-efficient and feasible under ambient conditions. Xu's group developed a Solar Thermal Swing Adsorption (STSA) technique that achieved CO_2 capture and desorption by intermittently illuminating porous carbon monomer adsorbents (PCMs), eliminating the possibility for solvent evaporation in liquid-phase CO_2 adsorbents. PCMs with high mechanical strength was prepared by one-step carbonization of guanidinium-linked polymeric xerogels *via* a template-free method.[38] This adsorbent exhibited superior

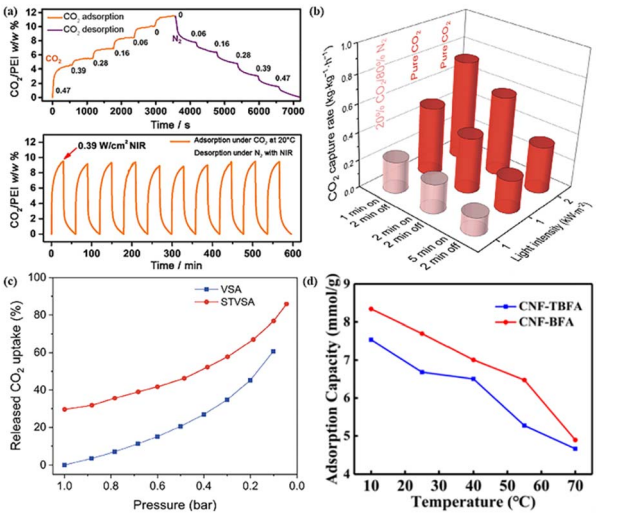

Fig. 5 (a) Stepwise CO_2 capture and release controlled by light irradiation with the change of power density (above); repeated light-triggered CO_2 adsorption/desorption (below). Reproduced with permission from ref. 37. Copyright 2017 *ChemSusChem*. (b) Comparison of CO_2 capture rate of PCM-1 under STSA conditions. (c) Released CO_2 at reduced pressure under VSA and STVSA conditions. Reproduced with permission from ref. 38. Copyright 2023 *Nano Research*. (d) Adsorption capacity of adsorbents at different temperature. Reproduced with permission from ref. 39. Copyright 2022 *Chemical Engineering Journal*.

CO_2 capture performance owing to its extensive ultrafine pores and elevated N-doping content. Additionally, the carbon-based framework exhibits excellent solar heat conversion and thermal conductivity. At a pressure of 0.2 bar, the CO_2 capture rate could reach 0.226 kg_{CO_2} kg_{carbon}^{-1} h^{-1} (Fig. 5b). Under the light intensity of 1000 mW cm^{-2}, the CO_2 desorption capacity reached 76.8% and 85.8% at 0.1 bar and 0.05 bar, respectively (Fig. 5c). Separately, He's group developed a heat-responsive, bionic fiber adsorbent (CNF-TBFA) with an ultra-low regeneration temperature of 60 °C for CO_2 desorption.[39] CNF-TBFA employed cellulose nanofibers (CNF) as the foundational skeleton, with the thermosensitive polymer poly(*N*-isopropylacrylamide) (PNIPAm), nano-graphene oxide (GO), and PEI amino functioning as the thermal response switch, photothermal conversion switch, and CO_2 adsorption site, respectively. As a result, CNF-TBFA demonstrated efficient solar energy utilization for regeneration and achieved a remarkable CO_2 adsorption capacity of 6.52 mmol g^{-1} under ambient conditions (25 °C and in the presence of water) (Fig. 5d).

Organic photothermal materials for CO_2 capture primarily include polydopamine (PDA) and thermoresponsive hydrogels.[44,45] For instance, through the self-polymerizing cross-linking of PEI and PDA, Gao *et al.* synthesized a PDA/PEI composite material. Following five sorption–desorption cycles, the material's average CO_2 regeneration efficiency was 93.4%.[41] (Fig. 6a). Inspired by the photoresponsive and low temperature regeneration properties of polymer gels, they combined nanogel particles (NGPs) containing *N*-[3-(dimethylamino) propyl] methacrylamide (DMAPM) with PDA to prepare a series of

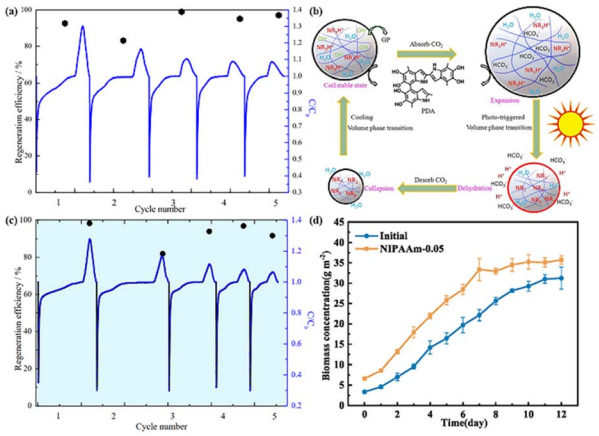

Fig. 6 (a) Cycle of CO_2 absorption and photo-induced desorption for the PEI/DP-1 and corresponding regeneration efficiency. Reproduced with permission from ref. 41. Copyright 2021 *Chemical Engineering Journal*. (b) Mechanism for reversible absorption of CO_2 by photo-triggered phase transition. (c) Normalized CO_2 absorption and photo-induced CO_2 desorption capacity of different samples. Reproduced with permission from ref. 42. Copyright 2023 *Chemical Engineering Journal*. (d) Growth curve of microalgal biofilm on the initial substrate and NIPAAm modified substrate. Reproduced with permission from ref. 43. Copyright 2023 *Environmental Research*.

composite polymers PDA@NGPs by the selfoxypolymerization process (Fig. 6b).[42] The CO_2 desorption rate of synthetic PDA@NGP was faster than NGPs, and it exhibited a volcano curve as the concentration of PDA in solution increases. Excessive PDA content could hinder light penetration, reducing solvent heating efficiency. Moreover, PDA@NGP1 maintained a high regeneration efficiency, averaging 92.45% over five consecutive CO_2 capture and release cycles (Fig. 6c).

Microalgae biofilms offer high photosynthetic efficiency and strong CO_2 capture capabilities. When grown on porous substrates, these biofilms benefit from the material's large specific surface area, yet mutual occlusion can limit light transmission to the biofilm's outer surface, hindering photosynthesis. To address this, Huang's group incorporated photoconductive particles (SiO_2) into a photosensitive resin and utilized 3D printing to fabricate a photoconductive, ordered porous photobioreactor (PBR).[43] This design expanded the effective adsorption area for microalgae by 13.6 times. A thermos-responsive hydrogel was further grafted onto the PBR's surface to create a temperature-responsive interface. The hydrogel's photothermal properties elevated the surface temperature, inducing contraction and hydrophobicity, which significantly enhanced microalgal cell adhesion. As a result, microalgae adsorption increased by 103%, and the growth rate reached 3.572 g m^{-2} d^{-1} (Fig. 6d). When the light source was turned off, the hydrogel surface temperature decreased, increasing hydrophilicity and facilitating the desorption of microalgae. This setup enabled effective temperature-controlled microalgae harvesting.

Nevertheless, the adsorption capacity and cycling stability of the aforementioned photothermal CO_2 capture materials are still inadequate. For adsorption capacity, the site density for CO_2 adsorption is limited by the amount of $-NH_2$ in amino compounds. Second, CO_2 diffusion may be spatially hampered by narrow MOFs channels. Thus, controlling the proper active site density and MOF pore size is a path that requires investigation.[46] In addition, there are the following issues with cycle stability and potential fixes. First, the regeneration of active sites is impacted by the density of photothermal sites, which restricts the desorption capacity of CO_2. By adjusting the percentage of photothermal materials, the ideal density of photothermal sites can be investigated. Second, pore collapse may occur in materials like hydrogels and MOFs over several cycles.[46] The preparation of materials with improved hydrothermal stability can increase the resilience of its structure. Thirdly, oxygen can inactivate the $-NH_2$ in amino materials to form $-NO_2$. To get rid of the extra O_2, the reactor itself must be vacuum-treated.[47,48] Fourth, in a humid environment, water molecules will occupy the pores of solid carbon materials, like PCMs, reducing their ability to adsorb CO_2. It is possible to decrease the competitive adsorption of water by correctly introducing hydrophobic groups. Additionally, water evaporation is unavoidable throughout the actual cycle capture process for liquid-phase CO_2 adsorbents, thus it's critical to promptly replace any lost water.

4. Photothermal technology for CO_2 methanation

4.1 Fundamentals of the photothermally catalytic CO_2 methanation

CO_2 is a chemically stable, linear, and symmetric molecule with a high C=O double bond energy of approximately 804 kJ mol^{-1} at 298 K. This stability renders CO_2 reduction thermodynamically unfavorable, typically requiring substantial energy input to initiate the reaction.[49] The eqn (1) is the chemical equation of CO_2 methanation proposed by Paul Sabatier.

$$CO_2\,(g) + 4H_2\,(g) \leftrightarrow CH_4\,(g) + 2H_2O\,(g) \quad \Delta H_{298K} = -165\ \text{kJ mol}^{-1} \tag{1}$$

At the same time, it is accompanied by the side reaction known as the reverse water–gas shift (eqn (2)).

$$CO_2\,(g) + H_2\,(g) \leftrightarrow CO\,(g) + H_2O\,(g) \quad \Delta H_{298K} = 41\ \text{kJ mol}^{-1} \tag{2}$$

The equation for CO_2 methanation highlights its reduced stoichiometric number and high exothermic enthalpy, indicating that the thermodynamic conversion is favored under higher pressures and lower temperatures. Below, we outline the principles and key differences among three distinct energy input methods.

Thermocatalytic CO_2 reduction requires a large amount of thermal energy input and appropriate catalyst activation.[50] Upon the activation by thermal energy, CO_2 molecules can surpass the energy barrier of activation energy to generate reaction intermediates, typically the pivotal step in the entire reaction. Furthermore, the desorption of the product is notably

significant, serving as a crucial step to facilitate the reaction's transition into the subsequent cycle and expedite the reaction rate.[51]

Photocatalytic CO_2 methanation is also considered to be an effective measure for the storage of renewable energy. The whole process consists of three key steps. In the first step, incident photons equal to or greater than the band gap energy of the photocatalyst are absorbed to generate electron–hole pairs. In the second step, the photogenerated electrons and holes migrate to the surface of the photocatalyst, respectively. In the migration process, a large number of photogenerated electrons and holes will be consumed. In the third step, photogenerated electrons reduce CO_2 to CH_4, while holes oxidize H_2 to H_2O.[52] However, because CO_2 is an inert molecule and CO_2 methanation involves multiple protons and electrons transfer, the development of photocatalytic CO_2 methanation has been limited. The conversion performance of CO_2 reduction photocatalysts reported in most studies is not very impressive.[53]

Photothermal CO_2 methanation, unlike photocatalysis and thermal catalysis, combines the strengths of both, emerging as a novel research area. Rather than a mere addition of photocatalytic and thermocatalytic effects, it functions as an integrated process where thermal acceleration enhances photocatalysis, and light amplifies thermal catalysis, achieving a synergistic outcome where the whole exceeds the sum of its parts.[28,51] This light-heat synergy enhances the system's ability to absorb light (including visible and infrared) and improves photothermal conversion efficiency. Additionally, it enables low-temperature CO_2 methanation in catalysts that typically require high temperatures, thus avoiding issues like catalyst agglomeration and deactivation.[32,54] In essence, photothermal CO_2 methanation reduces the high energy demands and catalyst degradation associated with traditional thermal catalysis, while also improving light energy utilization and CO_2 conversion rates over conventional photocatalysis. When the catalyst's reaction performance improves, its cost decreases while maintaining the same yield. As a result, photothermal technology can lower catalyst prices in addition to energy consumption costs.

4.2 Catalysts for photothermal CO_2 methanation

Plasmonic catalysts are currently the most widely used catalysts for photothermal CO_2 methanization.[55] These catalysts, typically composed of plasmonic metal nanoparticles, demonstrate a remarkable ability to induce collective oscillations of free electrons under light excitation. According to the characteristics of LSPR, reactions on plasmonic nanostructures fall into one of two groups: photothermal catalysis (photoexcited phonons) or plasmonic photocatalysis (photoinduced hot carriers). Plasmonic photothermal catalysis obviates the need for extra thermal energy input, as the inherent thermal reaction is powered by light, frequently exhibiting superior activity relative to conventional thermal catalysis. Furthermore, photoexcited hot carriers can selectively activate the Sabatier reaction by directly injecting into the chemical bonds of the adsorbed molecules, providing multiple avenues for improving the CH_4 selectivity.[55] Common plasmonic metals used in Sabatier reactions include noble metals (Au, Ru, Rh, *etc.*) and Group VIII metals (Ni, Co, *etc.*). Consequently, photothermal CO_2 methanation catalysts are categorized into noble metal and non-noble metal photothermal catalysts, each leveraging distinct photothermal mechanisms.

4.2.1 Noble metal-based photothermal catalysts. Ru-based catalysts stand out among other precious metal catalysts due to their exceptional stability and CO_2 methanation activity. However, the reactivity and light-absorbing capacity of metal Ru are significantly influenced by its morphology. For instance, Buskens' group synthesized both rod-shaped[56] and spherical Ru[57] by wet impregnation and loaded them onto γ-Al_2O_3, as depicted in Fig. 7a and b.[56] The rod-shaped Ru catalyst demonstrated 41.5% higher activity than its spherical counterpart at 150 °C and 8.5 Sun irradiance. This enhancement was attributed to the superior UV-Vis-NIR plasmonic resonance absorption properties of the rod-shaped nanoparticles (Fig. 7c). Similarly, Rohlfs *et al.* used wet impregnation to deposit Ru nanorods on γ-Al_2O_3 (Ru/γ-Al_2O_3) and conducted photothermal CO_2 methanation in a continuous flow system under focused light.[58] At an irradiance of 12.5 Sun, the CO_2 conversion rate surpassed 97%, with CH_4 selectivity reaching 100% and a CH_4 yield of 261.9 mmol g_{Ru}^{-1} h^{-1}, maintaining stability over 12 hours (Fig. 7d). The CH_4 yield increased exponentially with light intensity, emphasizing that photothermal heating was the primary driver of the reaction (Fig. 7e).

Researchers have further optimized the activity, selectivity, and stability of Ru-based catalysts by designing carriers with high specific surface areas and oxygen vacancies.[62] Titanate nanotube semiconductors (TiNTs), known for their substantial surface area and unique one-dimensional (1D) morphology.[63] Baldovi *et al.* synthesized Na, H/TiNT (Na, H/Ti_3O_7) through

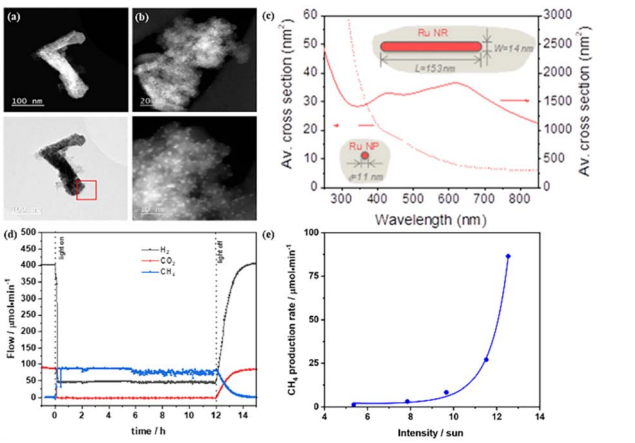

Fig. 7 (a) TEM and EDX mage of rod-shaped Ru on Al_2O_3. (b) TEM mage of spherical Ru on Al_2O_3. Reproduced with permission from ref. 56. Copyright 2020 *ChemCatChem*. (c) Calculated UV-vis-NIR extinction cross section of a single spherical Ru nanoparticle and a single Ru nanorod embedded in a γ-Al_2O_3 medium (inset: scale depiction of both nanoparticle types). Reproduced with permission from ref. 57. Copyright 2019 American Chemical Society. (d) CH_4 yield change over time at 12.5 sun. (e) CH_4 yield as a function of light intensity. Reproduced with permission from ref. 58. Copyright 2022 *Catalysis*.

a hydrothermal process, followed by ion exchange to produce Ru/TiNT-X, where Ru^{3+} ions were incorporated into TiNT.[59] Below 200 °C, the Sabatier reaction on Ru/TiNT was primarily driven by photochemical processes, while the thermal catalytic effect became more pronounced as the temperature increased (Fig. 8a). Under simulated illumination of 150 mW cm^{-2} and a temperature of 210 °C, the CH_4 yield reached 12 mmol g^{-1} h^{-1}, demonstrating both thermal and photochemical contributions to CO_2 methanation (Fig. 8b). Ru NPs in this composite absorb visible and near-infrared light, activating a plasmonic effect that converts photon energy into localized heat and hot electrons. Simultaneously, TiNT absorbs ultraviolet light, generating electron–hole pairs, with the resulting electrons transferred to Ru NPs, thus enhancing photocatalysis through efficient charge separation and transfer.

Similarly, Dong *et al.* prepared defective TiO_x by laser bombardment, and achieved uniform loading of Ru on the surface of TiO_x NPs through adsorption and photo-reduction.[60] Defective TiO_x NPs exhibited superior light absorption and enhanced photothermal conversion efficiency compared to TiO_2.[64] Across diverse catalysts and light sources, Ru–TiO_x exhibited exceptional performance, achieving the highest CH_4 yield at 15.84 mmol g^{-1} h^{-1} with an impressive selectivity of 99.99% (Fig. 8c). Notably, this result marked a substantial 176-fold increase compared to the CH_4 yield of Ru–TiO_2, which was only 0.09 mmol g^{-1} h^{-1}. The introduction of oxygen vacancies was confirmed to enhance light absorption and photothermal conversion, playing a pivotal role in photothermal CO_2 methanation. Theoretical calculations revealed that both photogenerated and hot electrons, derived from photoelectric effects and the photothermal conversion of TiO_x, are transferred to its surface simultaneously, facilitating CO_2 decomposition into CO* and O*. Besides, Zhou's group synthesized $Ni_2V_2O_7$ *via* coprecipitation and then created Ru@$Ni_2V_2O_7$ composites with varying Ru contents through Ru photodeposition.[61] Among these, the 0.35Ru@NVO sample demonstrated exceptional performance under a light intensity of 2 W cm^{-2}, achieving the highest activity with an average CH_4 yield of 114.9 mmol g^{-1} h^{-1}. This result outperformed both thermal catalytic activity and photocatalytic activity by 9.2 times and 6.6 times, respectively, and even surpassing their combined sum of the two by 3.9 times (Fig. 8d).

MOF has been widely used in photocatalysis, especially in the production of solar fuel, because of their porous and adjustable structure, high specific surface area, controllable acid–base distribution or metal nodes, and excellent electron–hole separation efficiency.[67] Photocatalysis of Sabatier reaction with MOF is a relatively new research field. By combining organic ligands and inorganic metals, Sabatier reaction photocatalysts with excellent energy band and photocatalytic stability could be constructed.[68] In 2020, Wang *et al.* synthesized the first Ti-IPA MOF (MIP-208) with high crystallinity and adjustable size by using Ti-based MOFs prepared with isophthalic acid (IPA) as the framework. By photo-deposition of RuO_x on MIP-208, the photocatalytic CH_4 production efficiency was increased by 20 times (Fig. 9a). At visible light and a temperature of 200 °C, MIP-208@RuO_x composites had the CH_4 yield of 0.8 mmol g^{-1}, the selectivity of 100%, and the high stability (154 h) (Fig. 9b). Then, in 2022, Cabero-Antonino *et al.* developed the MOF photocatalyst based on MIL-125(Ti)-NH_2 and loaded Ru NPs (RuO_x/MIL-125(Ti)-NH_2).[66] At a temperature of 200 °C and simulated sunlight, the highest methane yield (18.5 mmol g^{-1} after 22 hours) was achieved in a batch reactor, with stability demonstrated for up to 220 hours (Fig. 9c and d). The efficiency can be further improved on mixed metal MOFs. For instance, in 2023, Cabero-Antonino and colleagues expanded upon their previous

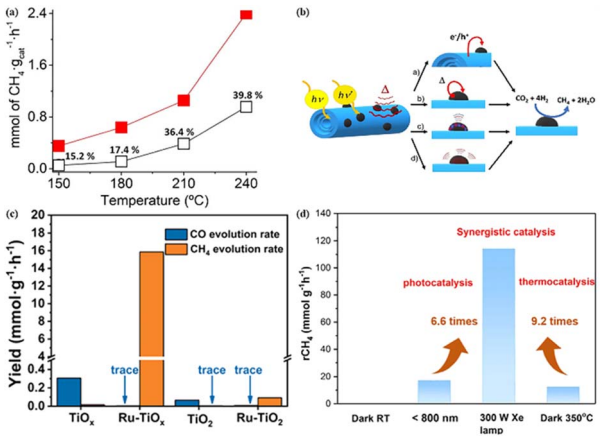

Fig. 8 (a) Methane conversion rate for Ru/TiNT-3.5 under 100 mW cm^{-2} light power (■) and in the dark (□). (b) Scheme of the photothermal catalytic mechanism. Symbols description: *hν* UV light; *hν′*: VIS + IR light. Reproduced with permission from ref. 59. Copyright 2020 *Nanomaterials*. (c) The yields of photothermal co-catalytic CO_2 hydrogenation for catalysts under full-spectrum. Reproduced with permission from ref. 60. Copyright 2023 *Applied Catalysis B: Environmental*. (d) Average CH_4 production rates over 0.35Ru@NVO under different conditions. Reproduced with permission from ref. 61. Copyright 2021 *Joule*.

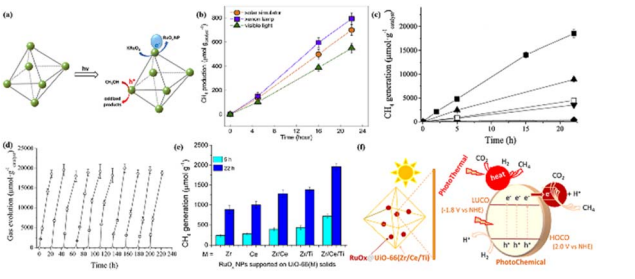

Fig. 9 (a) Simplified illustration of photodeposition of RuO_x NPs on MIP-208. (b) MIP-208@RuO_x CH_4 production under different light sources. Reproduced with permission from ref. 65. Copyright 2020 *Chem*. RuO_x@MIL-125(Ti)-NH_2 photothermal catalytic CO_2 methanation. (c) CH_4 yield maps at different temperatures under light and (d) stability test. 200 °C (■), 175 °C (▲), 165 °C (▼), 125 °C (◆); at 200 °C, H_2O exists (60 μL, □). Reproduced with permission from ref. 66. Copyright 2023 *Chemical Engineering Journal*. (e) Photocatalytic CH_4 generation using RuO_x NPs supported on UiO-66 solids under simulated sunlight irradiation at 200 °C. (f) RuO_x@UiO-66(Zr/Ce/Ti) photocatalytic H_2 reduction of CO_2 reaction mechanism. Reproduced with permission from ref. 15. Copyright 2023 *Chemical Engineering Journal*.

work by synthesizing polymetallic UiO-66 (Zr/Ce/Ti) composites and loading RuO_x nanoparticles.[15] The CH_4 productivity (1900 μmol g^{-1} after 22 hours) of the RuO_x NPs@UiO-66(Zr/Ce/Ti) composite at a temperature of 200 °C and simulated illumination was higher than that of comparable composites based on mono-metal and bimetallic composites. Moreover, the RuO_x NPs@UiO-66(Zr/Ce/Ti) composite showed better stability (Fig. 9e). The above three MOF-based photocatalysts all conformed to the dual reaction mechanism, including the photochemical mechanism based on electron–hole separation and the thermochemical mechanism where photon energy generated local hot spots to promote the photocatalytic reaction. Such as RuO_x NPs@UiO-66(Zr/Ce/Ti) composite, the reaction mechanism diagram showed that photoinduced electron transferred from HOMO of the terephthalate organic ligand to LUMO of the metal node and then to RuO_x NPs, thereby selectively reducing CO_2 to CH_4. RuO_x NPs was also able to convert light energy into heat energy through the photothermal effect, thus promoting the conversion of CO_2 to CH_4 (Fig. 9f). Although the activity was still far from the practical application of industry, the stability of CO_2 methanation catalyzed by photothermal catalysis of MOF-based composites was obvious.

Currently, integrating plasmonic metals with catalytically active metals to create "antenna-reactor" bimetallic heterostructures is regarded as one of the most effective approaches to enhance the catalytic activity of plasmonic nanostructures. Mateo *et al.* utilized impregnation and chemical reduction methods to deposit Au and Ru NPs onto a Siralox@ substrate (Au–Ru–S), respectively.[69] When subjected to a temperature of 250 °C and an intensity of 100 mW cm^{-2}, the CO_2 methanation rate of the Au–Ru–S composite achieved 102 mmol g_{Ru}^{-1} h^{-1}, displaying a selectivity of 100% (Fig. 10a). By absorbing visible light to create heat and sending it straight to Ru NPs, Au NPs encouraged the creation of CH_4 (Fig. 10b). Similarly, The Kuang's group synthesized Au@AuRu plasmonic NPs with an AuRu alloy surface and immobilized them onto graphitic carbon nitride (g-C_3N_4). The resulting Au@AuRu/g-C_3N_4 catalyst enabled CO_2 hydrogenation *via* hot electron injection excited by light under mild conditions.[70] By altering the surface of Au NPs with a small amount of Ru, the product can be efficiently transferred from CO to CH_4. At a temperature of 150 °C and an intensity of 1.1 W cm^{-2}, the CH_4 yield of Au@AuRu/g-C_3N_4 reached 103 μmol g^{-1} h with the selectivity of 98.4%. This activity was 12 times and 2.6 times that of Au/g-C_3N_4 and Au@Ru/g-C_3N_4, respectively (Fig. 10c and Table 1). In addition, Au@AuRu/g-C_3N_4 could significantly prolong the lifetime of hot electrons due to its unique hot electron injection behavior, which significantly improve the catalytic efficiency of CO_2 hydrogenation (Fig. 10d).

Besides Ru, noble metals Rh also have CO_2 methanation activity. Liu's group prepared Rh/Al_2O_3 by wet impregnation and demonstrated that the light-enhanced reaction rate was not due to heat on the Rh NPs surface or plasmonic photothermal heating.[71] Instead, the hot electrons produced by the plasmonic selectively activated the CHO intermediates and accelerated the production of CH_4, which had minimal effect on the CO

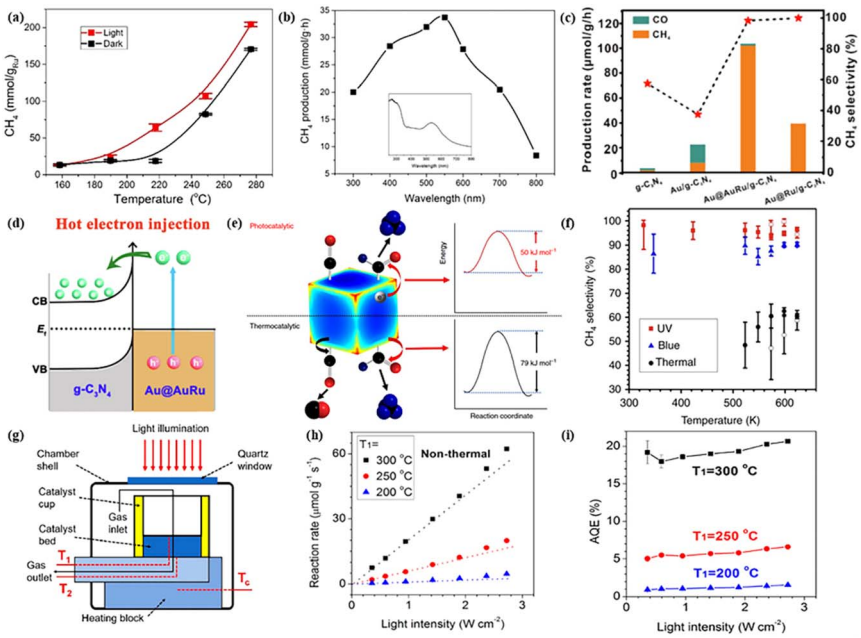

Fig. 10 (a) CH_4 evolution at different temperatures with use of the Au–Ru–S photocatalyst under irradiation or dark. (b) Photoresponse spectrum for the CH_4 production of Au–Ru–S after reaction. Reproduced with permission from ref. 69. Copyright 2018 *Chem. Eur. J.* (c) Production rates over different catalysts. (d) Schematic illustration of hot electron injection. Reproduced with permission from ref. 70. Copyright 2022 *Chemical Engineering Journal*. (e) Reaction mechanism on a rhodium nanocube. (f) Product selectivity on the rhodium photocatalyst. Reproduced with permission from ref. 71. Copyright 2017 *Nature communications*. (g) Schematic representation of the modified reaction chamber for *in situ* measurements. Nonthermal reaction rates of Rh/TiO_2 at different temperatures (h) and changes in AQE with I_{uv} (i). Reproduced with permission from ref. 72. Copyright 2018 *Nano Letters*.

Table 1 Representative photothermal catalysts for CO_2 methanation

Catalysts	H_2/CO_2 ratio	P (bar)	Light sources	T (°C)	CH_4 productivity	CH_4 sel. (%)	Reactor
Rod-shaped Ru/Al_2O_3 (ref. 56)	5 : 1	3.5	A solar simulator (Newport Sol3A), 0.1 W cm^{-2}	150	174 ± 9 mmol g_{Ru}^{-1} h^{-1}	100	Batch
Spherical Ru/Al_2O_3 (ref. 57)	5 : 1	3.5	A solar simulator (Newport Sol3A), 0.62 W cm^{-2}	220	5.09 mol g_{Ru}^{-1} h^{-1}	100	Batch
Ru/γ-Al_2O_3 (ref. 58)	4.5 : 1	1	Solar light simulator (Newport Sol3A), 1.25 W cm^{-2}		261.9 mmol g_{Ru}^{-1} h^{-1}	100	Flow
Ru/TiNT[59]	4 : 1	1.2	Irradiation with simulated sunlight of 150 mW cm^{-2}	210	12.4 mmol g^{-1} h^{-1}	>99	Batch
Ru-TiO_x (ref. 60)	4 : 1	1	300 W Xe lamp, 1 W cm^{-2}		15.84 mmol g^{-1} h^{-1}	99.99	Batch-50 mL
0.35%Ru@$Ni_2V_2O_7$ (ref. 61)	4 : 1		300 W Xe lamp, 2 W cm^{-2}		114.9 mmol g^{-1} h^{-1}	99	Batch-370 mL
MIP-208@RuO_x (ref. 65)	4 : 1		A Xe lamp (150 W) or a solar simulator	200	36.36 μmol g^{-1} h^{-1}	100	Batch-51 mL
RuO_x@MIL-125(Ti)-NH_2 (ref. 66)	4.2 : 1	1.3	Hg–Xe lamp of 150 W with an AM 1.5G filter	200	0.84 mmol g^{-1} h^{-1}	100	Batch-51 mL
RuO_x@UiO-66(Zr/Ce/Ti)[15]	4.2 : 1	1.3	Hg–Xe lamp of 150 W with an AM 1.5G filter	200	0.082 mmol g^{-1} h^{-1}	100	Batch-51 mL
Au–Ru–S[69]	4 : 1	1.3	300 W Xe lamp, 100 mW cm^{-2}	217.6	47.2 mmol g_{Ru}^{-1} h^{-1}	100	Bath-51 mL
Au@AuRu/g-C_3N_4 (ref. 70)	3 : 1	10	300 W Xe lamp, full spectrum, 1.1 W cm^{-2}	150	103 μmol g^{-1} h^{-1}	98.4	Batch
Rh/Al_2O_3 (ref. 71)	5.5 : 1	1	White light 3 W cm^{-2} (Prizmatix, UHP-F)			>90	Flow
Ni/80Ce–20Ti-SG[79]	4 : 1	0.75	300 W Xe lamp		17 mmol g^{-1} h^{-1}	100	Batch-540 mL
Ni/$Ce_xTi_yO_2$ (ref. 73)	4 : 1	0.75	300 W Xe lamp		0.88 L g^{-1} h^{-1}	100	Batch-540 mL
Ni/Nb_2C[74]	1 : 1	1	300 W Xe lamp		8.50 mol g_{Ni}^{-1} h^{-1} (CO and CH_4)		Batch
SA Ni/Y_2O_3 (ref. 86)	4 : 1	1	A Xe lamp (Microsolar 300) with an AM 1.5AG filter		7.5 L m^{-1} h^{-1}	100	Flow
Ni–TiO_2 (ref. 80)	3.8 : 1	1	300 W Xe lamp, 1.2 W cm^{-2}	325	95.7 mmol g^{-1} h^{-1}	99	Flow
Ni–$BaTiO_3$ (ref. 75)	4 : 1	5	300 W Xe lamp, 293 mW cm^{-2}		103.7 mmol g^{-1} h^{-1}	99	Batch-58 mL
NiO_x/La_2O_3@TiO_2 (ref. 76)	4 : 1	1	Visible light illumination, >420 nm, 390 mW cm^{-2}	250	21.9 mol_{CO_2} g^{-1}		Flow
Ni NPs[77]	4 : 1		12 W cm^{-2}		0.09 mmol g^{-1} h^{-1}	99.9	Batch-40 mL
$Co_7Cu_1Mn_1O_x$(200)[82]	3 : 1	1	A 300 W Xe lamp (234 mW cm^{-2}, 300–1100 nm)	200	14.5 mmol g^{-1} h^{-1}	85.3	Flow
0.16%Ir–CoO/Al_2O_3 (ref. 17)	4 : 1	1	A 300 W Xe lamp (420–780 nm; 2 W cm^{-2})	250	128.9 mmol g^{-1} h^{-1}	92	Flow

(desorption) production of co-metallic bonds. This conclusion was based on the assumption that thermal reactions and light reactions had the same basic steps and surface intermediates. In addition, the plasmonic effect of rhodium NPs could also reduce the activation energy of CO_2 methanation, resulting in the photocatalytic CH_4 yield of the catalyst exceeding the thermal catalytic CH_4 yield at 350 °C (Fig. 10e and f). Subsequently, Liu's group proposed the way to distinguish between the thermal and non-thermal contributions of plasmon-enhanced catalysts.[72] By measuring the total reaction rate and the top and bottom surface temperatures of the catalyst bed simultaneously, the effective thermal and non-thermal reaction rates under light were calculated (Fig. 10g). The non-thermal reaction rate of the plasmonic-enhanced reaction increased super-linearly with the increase of light intensity, while the apparent quantum efficiency (AQE) remained relatively insensitive to light intensity (Fig. 10h and i). The AQE on the Rh/TiO_2 catalyst at a temperature of 350 °C was calculated to be ~46%. The synergies between light and heat showed that the overall non-thermal efficiency of plasmonic-enhanced catalysis increased with the increase of temperature.

4.2.2 Non-noble metal-based photothermal catalysts. Given the high cost and limited availability of noble metals, the pursuit of economical and abundant photothermal materials holds considerable importance. Transition metals within Group VIII have emerged as promising candidates due to their enhanced light absorption capacity, positioning them as viable alternatives to noble metals in photothermal applications.[78] Because of its superior photothermal CO_2 methanation activity and stability, metal Ni has emerged as the most promising metal to replace precious metals. For instance, Amal's group synthesized cerium–titanium mixed oxide (*x*Ce–*y*Ti) using the sol–gel method, subsequently loading Ni through wet impregnation (Ni/*x*Ce–*y*Ti-SG).[79] Compared with rich titanium carriers, those rich cerium carriers exhibited higher absorption in the visible and near-infrared regions, which attributed to the fact that the presence of cerium improved dispersion of Ni metal. Additionally, moderate titanium doping contributed to the formation of oxygen vacancy defects, and an increased oxygen vacancy concentration after Ti doping further enhanced the methane yield. On this basis, Amal's group modified the sol method to prepare $Ni/Ce_xTi_yO_2$ catalyst.[73] In the batch photothermal reactor system, Ni/CeO_2 achieved the highest conversion rate, reaching 93% CO_2 conversion in approximately 60–90 minutes. The exothermic nature of the CO_2 methanation reaction could further elevate the catalyst's temperature, promoting the subsequent reduction of nickel and the generation of methane, thereby initiating a "snowball" effect. Typically, the effectiveness of photothermal catalysis is governed by three interconnected factors: (i) reactor temperature; (ii) reducibility of nickel; and (iii) exothermic attributes of the CO_2 methanation reaction. The combined effect of these three factors instigates a pronounced "snowball" effect that advances the photothermal conversion of CO_2 (Fig. 11a).

Furthermore, Wang's group reported the development of MIL-125 (TiMOFs)-derived titanium dioxide, which was subsequently loaded Ni NPs to form $Ni–TiO_2$.[80] At a temperature of 325 °C and a power density of 1200 mW cm^{-2}, the CH_4 yield reached 95.7 mmol g^{-1} h^{-1} with a selectivity of 99%. This activity was 2.7 times higher than that of dark conditions (Table 1). The catalyst also exhibited good stability (32 h). The photothermal effect enhanced the electron density of Ni, facilitating hydrogen dissociation. Moreover, the catalyst's good photoelectric conversion ability generated more photogenerated carriers and minimized carrier recombination.

MXenes are a class of two-dimensional transition metal carbides and nitride. Due to their electromagnetic wave absorption ability and LSPR effect, MXene materials (especially carbides) generally show excellent photothermal conversion properties.[81] He's group reported the discovery of MXene materials as superior photothermal carriers for metal NPs.[74] Ni/Nb_2C nanosheets with fewer layers were synthesized by hydrothermal method. In the absence of external heating, the CO_2 conversion of Ni/Nb_2C reached 8.50 mol g_{Ni}^{-1} h^{-1} (Fig. 11b). It was proved that MXene material could enhance the photothermal effect and improve the photothermal catalytic activity of Ni NPs.

Perovskite oxides have shown tremendous potential in photocatalytic CO_2 reduction due to their flexibility in composition and structure, as well as excellent charge separation efficiency. Gascon's group prepared the $Ni–BaTiO_3$ composite (Ni–BTO) by wet impregnation.[75] Under UV-visible-IR irradiation, the catalyst could reduce CO_2 to CH_4 with nearly 100% selectivity, and CH_4 yields up to 103.7 mmol g^{-1} h^{-1} (Table 1). The mechanism study showed that the non-thermal electron-driven pathway was dominant in the co-existing reaction, and the thermal contribution to the photothermal process is less (Fig. 11c). Electron-lattice collisions induced by light ultimately produce heat in metal nanoparticles, influencing catalytic activity akin to conventional thermal catalysis.

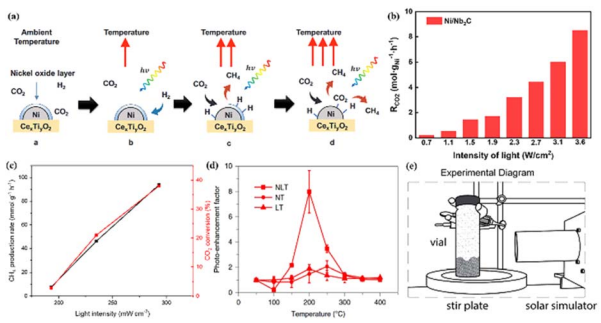

Fig. 11 (a) Photothermal methanation reaction process. Reproduced with permission from ref. 73. Copyright 2018 *Progress in Natural Science: Materials International*. (b) Photothermal catalytic activity under different illumination conditions. Reproduced with permission from ref. 74. Copyright 2021 *ACS Nano*. (c) CH_4 production rate (black) and CO_2 conversion (red) of Ni (5)-BTO as a function of light intensity. Reproduced with permission from ref. 75. Copyright 2021 *Advanced Functional Materials*. (d) Photo-enhancement factor of NiO_x/La_2O_3@TiO_2 (NLT), NiO_x/TiO_2 (NT) and La_2O_3@TiO_2 (LT) catalysts. Reproduced with permission from ref. 76. Copyright 2020 *Nature catalysis*. (e) A symbolic diagram of the reaction set-up. Reproduced with permission from ref. 77. Copyright 2021 Royal Society of Chemistry.

Besides, Scott's group used *in situ* isotope spectroscopy to isolate rate-determining intermediates in the light-assisted Sabatier reaction and found that the formic acid adsorbent (HCO_2^*) at $NiO_x/La_2O_3@TiO_2$ showed the eight-fold light enhancement after light activation (Fig. 11d).[76] The observed photo-enhancement depends on the presence of La_2O_3. On the one hand, it strongly interacts with the NiO_x catalyst, increasing the dispersion of NiO_x and lowering the reduction temperature. On the other hand, it utilizes oxygen vacancies on TiO_2 as proxy adsorption sites for CO_2. With the assistance of La_2O_3, NiO_x sites functions the primary sites for H_2 activation and photoactivation.

Previous studies have conventionally involved dispersing the active metal on the carrier instead of directly utilizing nanopowders of the active metal. Steeves *et al.* proposed a preliminary study of the photothermal Sabatier reaction on suspended nickel nanoparticles, demonstrating that particle isolation of simple ball-milled Ni NPs could enhance photothermal catalysis (Fig. 11e).[77] Then, they hypothesized that particle isolation and the high thermal gradient led to enhanced reaction performance. The batch reaction produced CH_4 at a rate of 1.3 mmol h^{-1} at the light intensity of 12 kW m^{-2}. Their study provides the basis for further research on multiphase catalysis of carrier-free NPs.

Other Group VIII transition metals are also frequently employed in photothermal CO_2 methanation, in addition to Ni. In 2021, Liu's group synthesized different ratios of Co–Cu–Mn trimetallic catalysts by the co-precipitation method.[82] At a temperature of 200 °C and a reactant concentration of 10% CO_2/30%H_2/60%N_2, the CH_4 yield produced by the Co_7Cu_1-Mn_1O_x catalyst was 14.5 mmol g^{-1} h^{-1}. Upon increasing the reactant concentration to 25% CO_2/75% H_2, the CH_4 and C_{2+} yields increased to 15.9 and 7.5 mmol g^{-1} h^{-1}, respectively (Fig. 12a and b). The presence of Cu in the catalyst regulated the reduction characteristics, balanced the Co^{2+} and Co^{3+} levels, and reduced the reduction temperature. Meanwhile, Mn_2O_3 contributed lewis acid sites that improved the adsorption capacity for CO_2 and H_2. The semiconductor Co_3O_4 and Mn_2O_3 generated a local hot spot due to rapid electron–hole recombination under light. Therefore, the synergistic effect of light and heat played a crucial role in enhancing the CO_2 methanation reaction for the Co–Cu–Mn trimetallic catalyst.

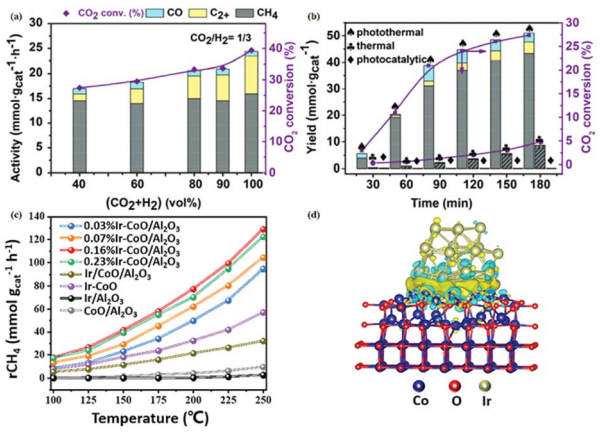

Fig. 12 (a) Effect of the total concentration of CO_2 and H_2 on the catalytic performances. (b) Catalytic performance test of Co_7Cu_1-Mn_1O_x (200). Reproduced with permission from ref. 82. Copyright 2021 *Green Chem.* (c) Effect of temperature on CH_4 yield rate over Ir–CoO, Ir/Al_2O_3, CoO/Al_2O_3, Ir–CoO/Al_2O_3 and Ir/CoO/Al_2O_3 catalysts. (d) Side view of the charge density difference for Ir–CoO. The cyan and yellow areas represent electron depletion and accumulation, respectively. Reproduced with permission from ref. 17. Copyright 2023 *Advanced Science*.

In 2023, Wang's group synthesized CoAl-LDH by hydrothermal method and then loaded Ir on CoAl-LDH to obtain Ir–CoO/Al_2O_3 catalyst.[17] The reference catalyst Ir/CoO/Al_2O_3 was prepared by directly loading Ir onto CoO/Al_2O_3. At the temperature of 250 °C and the light intensity of 2 W cm^{-2}, the CH_4 yield of the Ir–CoO/Al_2O_3 catalyst reached 128.9 mmol g^{-1} h^{-1}, with a selectivity of 92%, and a stability of 30 hours. In contrast, the CH_4 yield of the Ir/CoO/Al_2O_3 catalyst was only 32 mmol g^{-1} h^{-1}, significantly lower than that of the Ir–CoO/Al_2O_3 catalyst (Fig. 12c). This emphasizes the crucial role of efficient preparation of Ir–CoO interfaces for excellent catalytic performance. Density functional theory (DFT) calculations revealed electron transfer from CoO to Ir nanoparticles, facilitating H_2 dissociation. Moreover, CoO served as "nanoheaters" elevated the local temperature of the active site and thereby enhanced the photothermal catalytic activity (Fig. 12d).

Overall, photothermal CO_2 methanation research has advanced quite nicely. But when it comes to practical use, these photothermal catalysts still have issues with long-term stability. The following aspects can be considered. (1) Intrinsic design of the catalyst. During the actual reaction process, photothermal catalysts may face issues such structural collapse and obstruction, carbon deposit coverage, and active site sintering. First, the catalyst's inherent structure can be reinforced. This can be accomplished by optimizing the dispersion of metals, increasing the interaction between metal particles and the carrier, and creating high-entropy alloys to stop metal sintering and agglomeration.[83,84] Second, suitable interface and surface engineering can be built. The anti-carbon deposit ability and the concentration of active sites can be improved by maximizing the carrier's oxygen vacancy concentration and creating bimetallic or multimetallic interfaces.[85] (2) Reaction condition control. First, to guarantee that the reaction enters a balanced state and prevent carbon deposits, the proportion and flow rate of the raw gas should be in line with the photothermal catalyst's real conversion capacity. Second, to avoid photothermal catalyst aggregation and sintering, a reasonable control of outdoor light intensity and temperature is required. Thirdly, improving reaction activity and stability also requires a sensible photothermal reactor design. In Section 6.1 of this review, this subject is covered in further detail.

5. Photothermal technology for CO_2 capture and methanation

The process of converting captured CO_2 to CH_4 involves considerable labor and material costs. By adsorbing CO_2

straight onto the catalyst and turning it into CH_4, the Integrated Carbon dioxide Capture and Utilization (ICCU) offers a workable solution, removing the need for CO_2 desorption, transportation, and storage while significantly lowering the cost of large-scale industrial applications. Catalysts with both efficient CO_2 adsorption and rapid conversion capabilities are known as dual-function materials (DFMs).[87] DFMs are increasingly prominent in thermal catalysis, primarily for high-temperature CO_2 capture and *in situ* utilization using affordable adsorbents and widely available catalysts. Common DFMs for CO_2 capture and methanation include CaO–MgO composites[88] and Ni–MgO–Al_2O_3.[89] Additionally, the incorporation of alkali metal salts (AMS) has been shown to substantially enhance DFM performance.[90] However, thermal catalysis remains an expensive and energy-intensive process for ICCU. The integration of photothermal technology into ICCU has potential to further reduce CO_2 emissions and energy consumption, making the approach more sustainable and economically viable.

There are currently no reports of photothermal CO_2 methanation DFMs employing H_2 as a reducing agent. However, there have been a few reports of H_2O as a reducing agent. One of the most popular study areas at the moment is the synthesis of hydrocarbons from photothermal CO_2 and H_2O. In addition to lowering carbon emissions, it can use inexpensive raw materials to create high-value goods. Photothermal catalysts that convert CO_2 and H_2O mostly use semiconductors like TiO_2, In_2O_3, ZnO, and SiC as carriers. Metals like Au, Pt, Pd, Cu, Ni, and Co are then loaded into these catalysts.[93–95] The effectiveness of charge separation can be further increased by forming heterojunctions between these common carriers and metal complexes.[96] In the absence of sacrificial agents and focused light, the CH_4 generated by photothermal CO_2 and H_2O conversion typically ranges from 3 to 50 μmol g^{-1} h^{-1}.[97,98] The yield of CH_4 will rise significantly if concentration conditions are introduced, typically surpassing 100 μmol g^{-1} h^{-1}.[93,99] Research on photothermal CO_2 capture and methanation DFMs with water as the reducing agent is now in its infancy and is primarily conducted in reaction circumstances devoid of concentrated light and sacrificial agents. For instance, in 2019, Yu's group constructed a heterojunction material (CNNA/rGO) of highly crystalline carbon nanorods ordered on graphene, which improves light absorption, CO_2 capture, and interfacial charge transfer (Fig. 13a).[91] With pure light and H_2O as a reducing agent, CNNA/rGO's total CO_2 conversion and CH_4 yield were 12.63 μmol g^{-1} h^{-1} and 4.3 μmol g^{-1} h^{-1}, respectively. Furthermore, the isosteric heat of adsorption of the catalyst is 55.2 kJ mol^{-1}, and its CO_2/N_2 selectivity can reach 44 (Fig. 13b). By anchoring $ZnIn_2S_4$ (ZIS) nanowalls on the surface of nitrogen-doped graphene foam (NGF) in 2020, Liu's group created the mixed-dimensional composite ZIS/NGF using a hydrothermal method.[92] This material shows greatly improved photothermal conversion capabilities, selective CO_2 capture, and solar-driven CO_2 photoreduction. The ZIS/NGF1 composite with 1.0 wt% NGF has a CO_2-to-N_2 selectivity of 30.1, and its isosteric heat of CO_2 adsorption is approximately 48.2 kJ mol^{-1} (Fig. 13c and d). Under light exposure, the ZIS/NGF composite's yields of CH_4, CO, and CH_3OH were 9.1, 3.5, and 5.9 times higher than those of ZIS alone. Additionally, amino-functionalized semiconductors have shown promise in enhancing CO_2 capture and photocatalytic reduction. Xue's group notably increased CO_2 adsorption and chemisorption-based photocatalytic activity by amino-functionalizing TiO_2 and ZnO.[100,101] The amine group facilitates CO_2 activation by bonding "C–N" to form reactive carbamates. MEA–TiO_2 produced CH_4 (8.61 ppm h^{-1}) and CO (66.75 ppm h^{-1}) through *in situ* photoreduction, while MEA–ZnO yielded CH_4 (4.4 μmol g^{-1}) and CO (25.3 μmol g^{-1}).

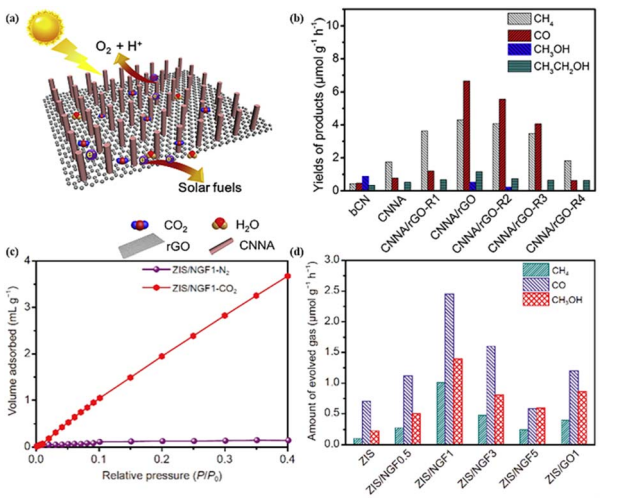

Fig. 13 (a) Proposed mechanism for CO_2 photoreduction of CNNA/rGO. (b) Photocatalytic CO_2-reduction property of catalysts at various amount of rGO in water vapor-saturated wet CO_2 gas. Reproduced with permission from ref. 91. Copyright 2019 *Joule*. (c) Adsorption isotherms of CO_2 and N_2 on CNNA/rGO at 273 K and 1 atm. (d) Comparison of different samples in CO_2 photoreduction products under simulated sunlight irradiation. Reproduced with permission from ref. 92. Copyright 2020 *Sci. China Mater.*

Despite the limited number of integrated CO_2 capture and methanation applications, the current research indicates that photothermal CO_2 capture and methanation has enormous potential. Nevertheless, photothermal CO_2 capture and photothermal CO_2 methanation operate at different temperatures. It is really important to figure out how to coordinate this issue. Currently, there are two primary types of photothermal CO_2 capture: liquid-phase adsorption and solid-phase adsorption. Photothermal CO_2 capture is often temperature-limited for this type of liquid-phase CO_2 adsorption, with temperatures typically not going over 90 °C. Both photothermal CO_2 capture and methanation can be combined by connecting them in series. The CO_2 desorbed from photothermal CO_2 capture can be sent directly to the photothermal CO_2 methanation reactor *via* a conduit. This form can still be used to reduce transportation and storage expenses for CO_2. Photothermal CO_2 capture and methanation can be coupled in two ways for the solid-phase adsorption of CO_2. The first method entails putting photothermal catalysts for CO_2 methanation and PCMs (photothermal CO_2 adsorbents) in a photothermal reactor. CO_2 released by PCMs and photothermal CO_2 methanation happen simultaneously under concentrated light. The second method

entails putting the DFMs for thermal CO_2 capture and methanation in a photothermal reactor and regulating the concentration intensity to supply the heat needed for these processes. While realizing fully integrated photothermal CO_2 capture and methanation systems remains a work in progress, advancing these technologies is essential for achieving cost and energy efficiency in large-scale applications.

6. Reactor design and techno-economic assessment (TEA)

Although significant progress has been made in the development of photothermal CO_2 capture and methanation materials, most catalysts remain limited to laboratory-scale applications. However, achieving the industrial production of CO_2 methanation is the ultimate goal. As a result, we need to assess the industrial production potential of photothermal CO_2 capture and methanation as well as optimize the reactor design. Here, we primarily go over the design of the reactor used for photothermal CO_2 methanation and perform a TEA of the commercial production of CO_2 capture and methanation using photothermal technology.

6.1 Reactor design

From the screening of photothermal catalysts to industrial applications, photothermal reactors are crucial. However, photothermal reactor design research is still in its infancy. The majority of researched photothermal CO_2 methanation reactors use flow gas and batch reactors, which are typically outfitted with temperature-raising adjustable reaction vessels and optically transparent windows. Quartz reactors, photothermal reactors, tubular quartz capillaries, and Harrick cell are examples of common photothermal reactors.[102] The majority of these photothermal reactors have size restrictions set at the milliliter level, and the mobile gas flow rate is capped at 10–30 mL min^{-1}. Batch reactors are challenging to use in industrialized production; mobile gas reactors, on the other hand, clearly offer greater potential. Consequently, the photothermal flow gas reactor's design and optimization represent a significant undertaking.

Up to now, photothermal reactors can be designed and optimized in three different strategies. Enhancing the reactor's photothermal conversion efficiency is the first strategy. A selective photoabsorber-based photothermal system was suggested by Ye's group.[108] Specifically, they coated the inside wall of the quartz tube with SA Ni/Y_2O_3 nanosheet catalyst for the CO_2 methanation reaction and coated the outside wall with a selective photoabsorber (AlN_x/Al foil layer) to absorb light from the outside (Fig. 14a). Under low solar radiation (1 kW m^{-2}), the photothermal system achieved temperatures up to 288 °C, which is three times greater than those of traditional photothermal catalytic systems. Similarly, Wang's group developed a photothermal system using Ti_2O_3/Cu film as the photothermal layer and BiO_x/CeO_2 as the catalyst layer.[109] Under 1 sun and 3 sun units of irradiation, BiO_x/CeO_2 can be heated to 314 °C and 470 °C, respectively. The photothermal system's CO production at 3

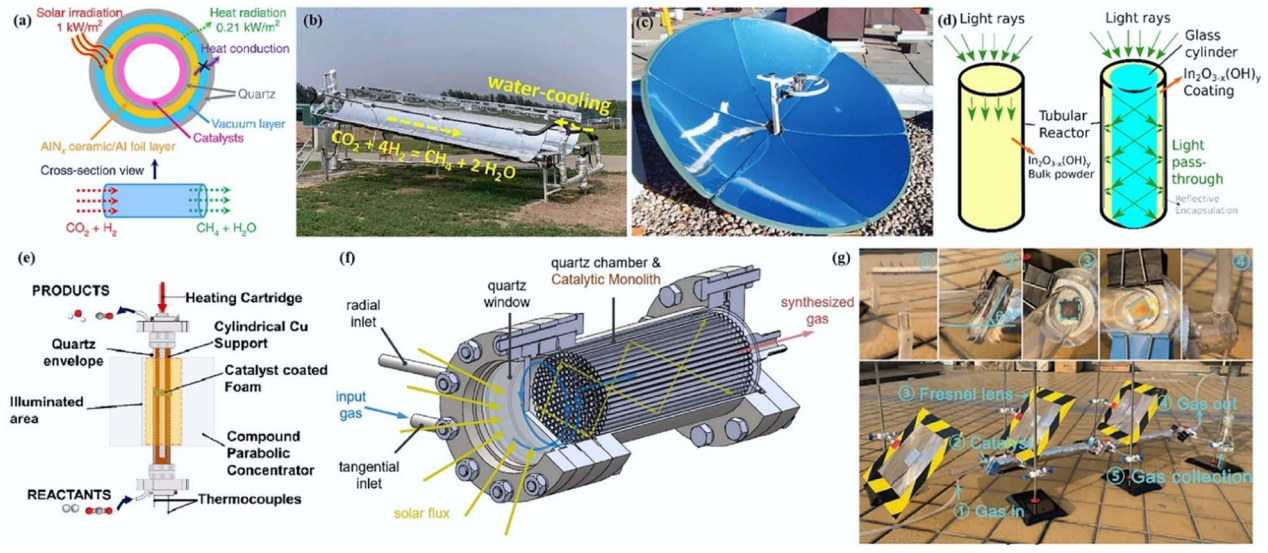

Fig. 14 Schematics for designing and optimizing photothermal reactors. (a) Schematic of the new photothermal system used for photothermal CO_2 methanation with the selective absorber and the catalysts. Reproduced with permission from ref. 86. Copyright 2019 *Nature Communications*. (b) Photograph of the outdoor self-operating photothermal CO_2 methanation system under solar irradiation. Reproduced with permission from ref. 103. Copyright 2025 *Energy Environ. Sci.* (c) The rooftop solar concentrator and reactor attached to it. (d) Schematic showing how light rays are not able to penetrate deeply through a packed powder tube in a tubular flow reactor, whereas light guiding distributes light throughout the coating. Reproduced with permission from ref. 104. Copyright 2021 *Nature Communications*. (e) Simplified scheme of the annular photoreactor employed in this work to conduct the photo- and thermal CO_2 hydrogenation on coated foams. Reproduced with permission from ref. 105. Copyright 2021 *Nature Communications*. (f) Solar receiver-reactor: reactor model with design components and schematic depiction of its operation. Reproduced with permission from ref. 106. Copyright 2022 *Chemical Engineering Journal*. (g) Optical images of flow reactor system outdoor, inset showed the enlarged partial components. Reproduced with permission from ref. 107 Copyright 2022 *Adv. Energy Mater.*

suns was 31.00 mmol g^{-1} h^{-1}, which is 4 times the greatest amount that the existing solar RWGS technology can create at 20 suns. In 2025, Ye's group went on to suggest an enhanced photothermal reaction system, using 2D $Ni_1Ce_1O_3$ as the catalyst and a TiC/Cu film as the photothermal layer. The catalyst's temperature can reach 352 °C under 1 sun. Remarkably, they also discovered that even after the light source was switched off, the heat generated by the CO_2 methanation reaction could sustain the entire system and keep the CO_2 conversion rate constant. Furthermore, the reaction system was enlarged for outdoor display (Fig. 14b), operated day and night for five consecutive outdoor periods, and eventually produced 10 tons of boiling water and 898 m^3 of CH_4.[103] Each of the three photothermal layers mentioned above has exceptional photothermal conversion capacities, and a robust CO_2 methanation reaction is triggered under 1 sun. It takes a large area of light irradiation and temperature management to operate this kind of photothermal reactor. Under experimental conditions, the photothermal layer on the quartz tube is typically irradiated all around using a mirror reflection box. In outdoor amplification devices, parabolic reflectors are typically used to provide the tubular reactor with all-around irradiation. As an illustration, for the TiC/Cu-based reactor, the catalyst temperature rised above 300 °C when the amount of light outside surpassed 0.2 kW m^{-2}.[103] The CO_2 methanation reaction proceeded rapidly and generated a significant quantity of heat, thus condensate water must be added to regulate the temperature. After CO_2 methanation has been effectively triggered, a decrease in the amount of light outside or even in the absence of light can still keep the CO_2 conversion rate almost constant for up to 84 hours. Consequently, there is a lot of industrial potential for using this kind of photothermal conversion reactor for CO_2 methanation reactions.

Enhancing the reactor's light efficiency is the second strategy. Using quartz waveguide as a substrate covered with $In_2O_{3-x}(OH)_y$ nanorods, Ozin's group was able to enhance the CO yield under visible light by 8.1–8.7 times (Fig. 14c).[104] When the light was switche' off, the system displayed persistent photoconductivity, which means it kept producing CO at the same rate for two hours. The uniform distribution of light intensity on the optical waveguide prevents the issue of photogenerated charge carrier recombination at high light intensities, and the internal reflection and scattering of the optical waveguide improve light utilization (Fig. 14d). Additionally, the research team used nickel foam as a coating foam inside the annular photoreactor (Fig. 14e).[105] The nickel foam's millimeter-sized holes allowed light to permeate the whole carrier, increasing the catalyst's rate of light usage. Its superior heat conduction capability also helped to distribute heat evenly. Under light enhancement, the system's CO generation rate can reach 130%. By increasing the depth of light penetration, the second type of photothermal reactor often increases the light utilization rate and is better suited for reaction systems where photocatalysis is the dominant process. Take quartz waveguides as an example. The light distribution will always become weaker from top to bottom as light is projected from its top, and the same is true for the temperature distribution. In contrast to the first type of photothermal reactor, which is completely exposed to light, the second form of photothermal reactor is more focused on longitudinal light transfer and can conduct experiments either indoors or underground.

The expansion of solar reception reactors is a third strategy. A direct solar receiving reactor with the ability to concentrate light and tolerate temperatures as high as 1000 °C was created by Bhatta *et al.* (Fig. 14f).[106] Because tubular quartz has a better light transmission than zirconia foam, they discovered that using tubular quartz as a catalyst carrier had a higher CO_2 conversion efficiency. Liu *et al.* combined a Fresnel lens with light-gathering properties and a Ru/Al_2O_{3-x}-L catalyst layer with periodic microchannels to create an integrated transient flow reactor system (Fig. 14g).[107] A lower volume CO_2 methanation reaction is supported by the local pressure that forms at the microchannel structure's edge, and a higher CO_2 conversion rate is promoted by the arrangement of repeated units. Under outdoor sunlight, the system achieved a CO_2 conversion of 27.10% and a CH_4 production of 18.00 mmol min^{-1}. Based on the designs of the first two types of photothermal reactors, the third type includes improvements and expansions. Expanding the reactor volume is the first method to be considered from the standpoint of increasing the reaction volume. The second strategy is to continue connecting the photothermal reactor units in succession in order to increase the reaction conversion rate.

Overall, there is a significant temperature dependence for the first kind of photothermal reactor that is dominated by thermal catalysis. In other words, a specific beginning light intensity is necessary to have enough thermal energy to start the reaction, and condensate water is required to regulate the temperature when the exterior light intensity is too high. The second kind of photothermal reactor, which is primarily based on photocatalysis, is highly dependent on the distribution of light. As light intensity diminishes, the reactivity also lowers, but the reactor is less temperature-dependent. Generally speaking, better light utilization and luminous flux are necessary for the construction of a photothermal reactor for CO_2 methanation, as is temperature control within the reaction's suitable range of 150–500 °C. As a result, the CO_2 methanation reaction cannot be conducted in a large-scale solar concentrating reactor designed for the reaction of CO_2 and H_2O.[110,111] Furthermore, the catalyst will deactivate and the selectivity of the reaction product will diminish due to the high temperature that results from high intensity solar concentrating.

6.2 TEA

We used economic evaluation models (corporate finance) to evaluate the economic viability of five distinct processes (A, B, C, D, and E) in order to determine the potential of photothermal technologies to lower CO_2 capture and methanation costs.[112] Table 2 displays the particular circumstances of the five procedures.

The net present value (NPV), levelized cost (LC), and other indicators are the primary components of TEA. NPV: estimates a project's lifetime cash flow and discounts it to its current value using time value. LC: the cost per unit of production, which is the total cost of the project divided equally among all charges. Table 3 displays the fundamental components required to determine the flat cost of photothermal CO_2 methanation.[23,113]

Table 2 Specific conditions for five different processes

	CO_2 source	CO_2 methanation method	Carbon subsidy
A	Purchase	Thermocatalysis	No
B	Purchase	Photothermal catalysis	No
C	CO_2 capture	Photothermal catalysis	No
D	Photothermal CO_2 capture	Photothermal catalysis	No
E	Photothermal CO_2 capture	Photothermal catalysis	Yes

These components primarily consist of the capital cost, production cost, operation and maintenance cost, and post-processing cost. The specific calculation formula is as follows:

$$\mathrm{NPV}(\mathrm{CF},\ \delta) = \sum_{t=1}^{T} \frac{\mathrm{CF}_t}{(1+\delta)^t} \tag{3}$$

where $\mathrm{CF} = (\mathrm{CF}_1, \mathrm{CF}_2, \ldots, \mathrm{CF}_T)$ is a vector to store the cash flow on each time slot t, δ is the depreciation rate, and T is the terminal time slot. In general, each CF_t can be calculated independently by the total revenue TR_t at t minus the total cost TC_t at t,

$$\mathrm{CF}_t = \mathrm{TR}_t - \mathrm{TC}_t \tag{4}$$

$$\mathrm{TR}_t = \sum_{n=1}^{N} {p_n}^t \cdot {q_n}^t + A \tag{5}$$

$$\mathrm{TC}_t = K_t + M_t + S_t + E_t + \sum_{m=1}^{M} {c_m}^t \cdot {q_m}^t \tag{6}$$

$$\mathrm{LC}(\mathrm{TC},\ \mathrm{TP},\ \delta) = \frac{\mathrm{NPV}(\mathrm{TC},\ \delta)}{\mathrm{NPV}(\mathrm{TP},\ \delta)} \tag{7}$$

$$\mathrm{TP}_t = \sum_{n=1}^{N} {q_n}^t \tag{8}$$

In eqn (4)–(6), N indicates the total number of the outcomes, and M indicates the total number of inputs. ${p_n}^t$ and ${q_n}^t$ represent the price and quantity of outcome n at time slot t. ${c_m}^t$ and ${q_m}^t$ represent the cost and quantity of input m at time slot t, where feedstocks and energy costs are contained in ${c_m}^t$. A_t, K_t, M_t, S_t, and E_t are the additional income, capital cost, maintenance cost, separation cost, and environmental cost, respectively. In eqn (7) and (8), TP is the total production.

With a three-month capital building cycle and a 10 year plant life, TEA's NPV and LC are computed. Table 3 presents price data, costs for maintenance and operation, and the cost of the assets used in a concise manner. The depreciation rate is assumed as 5%. It is projected that the plant can produce 200 tons of CH_4 annually with an 80% CO_2 conversion and 100% CH_4 selectivity using the present idealized Ni-based catalyst. The unreacted CO_2 in the product gas is recovered and reused by CO_2 capture.

The reactor needs to be heated and uses electricity when thermocatalytic CO_2 methanation is used.[23] The reactor needs electricity when thermal catalysis is used, and the electro-thermal conversion efficiency is 90%. When using photo-thermal catalysis, no additional electricity is needed because the concentrated light produces all of the heat. Furthermore, no specific studies have been carried out to examine the economics of photothermal CO_2 capture because it is still in the design and development stage. Assuming that light energy can substitute

Table 3 All costs used in the TEA case study

Cost type	Cost item		Cost (CNY)
Capital cost	Costs of equipment	Reactor	4000
		Compressor	37 500
		Extraction	3000
		CO_2 collector	5000
	Lab investment	Construction	100 000
Production cost	Feedstocks (RNY per ton)	Methane	2600
		Hydrogen	4000
		Carbon dioxide	400
Maintenance and operational costs	Energies	Electricity	0.6654[a,b] RNY per kWh
	Operations	Carbon dioxide capture cost	278.8 CNY per ton
	Maintenance	Equipment maintenance	0.2 Times capital cost
		Salaries	60 000 RNY[b]
		Rents	30 000 RNY
		Others	0.1 Times electricity cost
Post-processing cost	Environmental cost	Carbon market cost	786.6[c] RNY per ton

[a] The electricity price is assumed to be the July 2024 industrial electricity rate in Shanghai, China at 0.6654 CNY per kWh. [b] The scale of consideration pertains to a small-scale chemical company, assumed to be 10 000 times larger than the laboratory-scale case. The operational duration is established at 100 hours per week, encompassing 52 weeks per annum. [c] The carbon market price adopts the peak value observed in the European Union Emission Trading Scheme, set at 100 EUR per ton, equivalent to 786.6 CNY per ton.

electricity, the cost of photothermal CO_2 capture can be lowered to 17–22% of its initial cost.[114] To make calculations easier, we calculate the cost to be 20% of the initial cost.

The market price of CH_4 is 2600 RNY per ton, whereas Fig. 15a illustrates the LC of A, B, C, D, and E under five different conditions, which are 4708.8, 4573.7, 4184.2, 3350.2, and 1187 RNY per ton, respectively (Fig. 15a). Compared to the market price of CH_4, the LC of traditional thermocatalytic CO_2 methanation (A) is significantly greater. The issue of CO_2 methanation (B)'s high LC cannot be effectively resolved by catalyzing the process with solar energy rather than thermal energy. Utilizing a CO_2 absorber in place of buying CO_2 (C) can reduce raw material costs based on photothermal CO_2 methanation; nevertheless, the cost of CO_2 capture technology is still very high at the moment and has not decreased significantly. The constant use of power to produce heat energy is a significant portion of the cost of CO_2 capture and desorption technology, in addition to the consumption of CO_2 adsorbents. Fortunately, the cost of CO_2 collection could be significantly decreased if solar energy is used. Currently, photothermal CO_2 capture and desorption technology is the subject of numerous investigations. Here, we estimate that photothermal CO_2 capture technology (D) may be introduced at a cost 20% of the prior technology. As a result, the calculated LC has greatly decreased, albeit it is still more than the price of CH_4 on the market. Given that CO_2 emissions are tradable on the global carbon trading market, the LC that has been computed is much less than the market price of CH_4. This suggests that the cost of raw materials plays a major role in determining the LC. When it comes to carbon trading, the cost of carbon is 786.6 RNY per ton, which is sufficient to pay for CO_2 as a raw material and still have surplus. Consequently, we examined the NPV ratio of each cost under various conditions. What we discovered was that, under A–D conditions, the production cost accounted for over 80% of the proportion, and H_2 accounted for the largest share of the raw gas cost, reaching over 64% (Fig. 15b and c). The cheapest green hydrogen is water electrolysis hydrogen, but its LC is about three times that of traditional grey hydrogen. Even with our low-cost purchase, grey hydrogen still costs up to 4000 RNY per ton.[115] Under conditions C, D, and E, a sensitivity analysis of LC for CO_2 and H_2 raw gas costs was carried out (Fig. 15d and e). In condition C, LC will have a fluctuation differential of 205.6 RNY per ton when the price of CO_2 feedstock gas is altered. The LC fluctuation differential drops to 41.1 RNY per ton when photothermal CO_2 capture and/or carbon subsidies are included. In other words, LC will be slightly affected by changes in CO_2 prices when the price of CO_2 raw gas is sufficiently low. On the other hand, the price of H_2 makes up a far higher percentage of the raw gas cost. Consequently, the fluctuation difference of LC under conditions C, D, and E is all approximately 500 RNY per ton when the cost of H_2 is altered. The LC could decrease dramatically if hydrogen's price can be brought down.

Since raw material prices are typically far greater in actual industrial production than other costs, lowering the price of H_2 and CO_2 is essential to cutting LC. The technology for producing hydrogen is currently relatively mature. The most environmentally benign method of producing hydrogen is *via* electrolyzing water if the carbon emissions from the process of generating power are ignored. Furthermore, the primary cause of the high cost of hydrogen energy is linked to the transportation and storage infrastructure; these factors serve as a bottleneck, restricting the growth of the hydrogen energy sector.[7] Because there is currently no hydrogen production in locations that use hydrogen and hydrogen transport pipelines require major

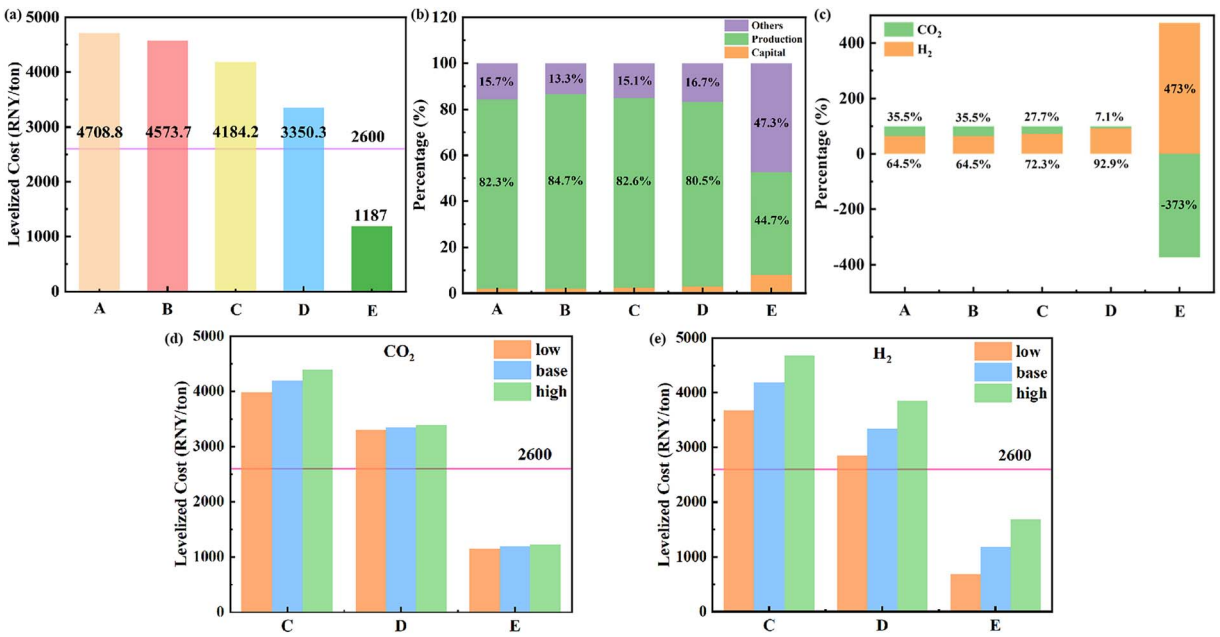

Fig. 15 Comparison of LC and NPV for five processes. (a) LC under different conditions. (b) The NPV ratio of capital costs, production costs and other costs under different conditions. (c) The NPV ratio of raw material cost under different conditions. Sensitivity analysis of LC under different CO_2 cost (d) and H_2 cost (e) (low: 0.8 times cost, base: 1 times cost, high: 1.2 times cost).

investment, high-pressure gas storage and transportation must be used temporarily, which significantly raises the cost of transporting hydrogen. Therefore, the key to lowering H_2 pricing is developing technologies for hydrogen storage and delivery as well as lowering the cost of using renewable energy. Thus, integrating the photothermal CO_2 capture and methanation plant with the electrolytic hydrogen production plant may immediately feed the generated CH_4 into the current natural gas transportation infrastructure while also drastically lowering the expenses associated with hydrogen storage and transportation. In the case of CO_2, it is economical and environmentally friendly to directly capture CO_2 from the air or industrial waste gas. The cost of carbon capture technology is presently somewhat high, but it may be significantly lower if light and other renewable energy sources are used.[112] As a result, the advancement of photothermal CO_2 capture technology has the potential to lower CO_2 pricing while simultaneously encouraging a decrease in CO_2 emissions. Furthermore, the required carbon subsidy policy is essential since it will, on the one hand, significantly lower the cost of CO_2 raw gas and, on the other hand, encourage the growth of the CO_2 reduction industrial chain. In short, lower CO_2 capture costs and enhancing carbon subsidy policies are significant strategies to lower CO_2 pricing.

Even while methanation and photothermal CO_2 collection are not economically feasible without carbon subsidies, the extra electricity produced by renewable energy sources similarly wastes resources if it is not stored. Electrical energy may be efficiently stored using PtG technology, and as CH_4 has a more developed transport system than H_2, it is thought to be the most feasible choice.[7] Photothermal CO_2 capture and methanation, in addition to PtG technologies, have shown promise in the aerospace field to support long-term space exploration missions and enhance the sustainability of space missions. To be more precise, the International Space Station electrolyzes water primarily to create O_2, with H_2 being released as exhaust. The production of CH_4 and H_2O from CO_2 and waste H_2 in the space station can accomplish resource recycling while simultaneously providing astronauts with clean, safe drinking water and producing methane fuel for rocket propulsion.[116] Consequently, it is crucial to advance photothermal CO_2 capture and methanation.

7. Conclusion and outlook

7.1 Conclusion

The high production cost remains a major barrier to the industrial application of CO_2 capture and methanation. This paper explores recent advancements in photothermal CO_2 capture and methanation technologies, focusing on strategies to reduce associated costs. It also provides a detailed introduction to the design and preparation of photothermal materials, experimental conditions and reactivity, photothermal reactor design, and the TEA in production process. Furthermore, the difficulties and future paths of photothermal CO_2 capture and methanation methods are discussed. In photothermal CO_2 capture, the material has the performance of light-driven CO_2 adsorption and desorption by combining photothermal conversion and CO_2 adsorption, and the CO_2 desorption ability can be regulated by adjusting the photothermal conversion ability of the material. In the photothermal CO_2 methanation reaction, photothermal synergism can accomplish $1 + 1 > 2$ catalytic activity. It is essential to construct photothermal reactors with greater light utilization and make them suitable for realistic industrial production in addition to producing more stable, affordable, and efficient photothermal materials. The use of photothermal technology in carbon dioxide capture and methanation has enormous promise, despite the fact that there is still much to be done.

7.2 Outlook

7.2.1 Photothermal CO_2 capture. Photothermal CO_2 capture materials are mainly composed of photothermal NPs (Ag, Fe_3O_4, PDA, *etc.*) and CO_2 adsorbents, followed by porous carbon-based materials with both CO_2 adsorption and photothermal conversion. According to these two types of materials, CO_2 adsorption can be divided into liquid-phase adsorption and solid-phase adsorption. (1) Liquid-phase CO_2 adsorption. First, controlling the amino compound's $-NH_2$ concentration and the photothermal material's doping ratio can improve the CO_2 adsorption and desorption capabilities of the photothermal CO_2 capture material. Second, controlling the pore structure and hydrothermal stability of CO_2 capture materials with frameworks like MOFs and hydrogels can improve their cycling stability. Thirdly, a higher temperature (about 90 °C) is normally needed for liquid-phase CO_2 adsorbents to desorb CO_2 efficiently, which usually encourages water evaporation. Thus, one approach is the development of photothermal CO_2 capture materials with low temperature CO_2 desorption properties. (2) Solid-phase CO_2 adsorption. Currently, this kind of photothermal CO_2 capture material is primarily made of carbon, and in order to lessen the competing adsorption of water, a suitable hydrophobic structure must be built. Although existing photothermal CO_2 capture materials can achieve CO_2 adsorption regeneration in a short cycle through light, their CO_2 regeneration capacity and stability are far from the commercial level. Therefore, it is necessary to develop more stable photothermal CO_2 capture materials, and expand the scale of experiments to explore the practical application value of photothermal CO_2 capture materials.

7.2.2 Photothermal CO_2 methanation. Photothermal CO_2 capture materials are mainly composed of photothermal NPs (Ag, Fe_3O_4, PDA, *etc.*) and CO_2 adsorbents, followed by porous carbon-based materials with both CO_2 adsorption and photothermal conversion. According to these two types of materials, CO_2 adsorption can be divided into liquid-phase adsorption and solid-phase adsorption. (1) Liquid-phase CO_2 adsorption. First, controlling the amino compound's $-NH_2$ concentration and the photothermal material's doping ratio can improve the CO_2 adsorption and desorption capabilities of the photothermal CO_2 capture material. Second, controlling the pore structure and hydrothermal stability of CO_2 capture materials with frameworks like MOFs and hydrogels can improve their cycling stability. Thirdly, a higher temperature (about 90 °C) is normally needed for liquid-phase CO_2 adsorbents to desorb CO_2 efficiently, which usually encourages water evaporation. Thus, one approach is the development of photothermal CO_2 capture materials with low temperature CO_2 desorption properties. (2) Solid-phase CO_2

adsorption. Currently, this kind of photothermal CO_2 capture material is primarily made of carbon, and in order to lessen the competing adsorption of water, a suitable hydrophobic structure must be built. Although existing photothermal CO_2 capture materials can achieve CO_2 adsorption regeneration in a short cycle through light, their CO_2 regeneration capacity and stability are far from the commercial level. Therefore, it is necessary to develop more stable photothermal CO_2 capture materials, and expand the scale of experiments to explore the practical application value of photothermal CO_2 capture materials.

7.2.3 Photothermal CO_2 capture and methanation. While photothermal CO_2 capture and methanation has potential, there isn't much research on combining the two at the moment. Nonetheless, the following combination approaches may be conceivable based on current research. For liquid-phase photothermal CO_2 capture, the two processes of photothermal CO_2 capture and photothermal CO_2 methanation can be linked. For solid-phase photothermal CO_2 capture, photothermal CO_2 capture and photothermal CO_2 methanation can take place in the same system. It can be accomplished in the two ways listed below. The first strategy involves combining solid-phase CO_2 adsorbents (such PCMs) with photothermal CO_2 methanation catalysts. The second strategy uses thermal catalytic CO_2 capture and methanation DFMs, where the reaction's heat is produced by concentrated light.

7.2.4 Design of photothermal reactor. (1) Photothermal conversion reactor dominated by thermal catalysis. Large-scale outdoor experiments have currently demonstrated the practical application value of this sort of reactor, but it also has a high temperature dependence. Thus, future research focuses on balancing temperature and light intensity. (2) Light conduction reactor dominated by photocatalysis. This sort of reactor's primary benefit is that it enhances light's longitudinal conduction and can even produce indoor photothermal reaction devices, whose reaction activity is heavily reliant on light distribution. Therefore, the goal of future study is to improve this reaction device's light conduction and light dispersal capabilities. Additionally, there are two primary methods for scaling up photothermal reactors: increasing reactor volume and linking unit reactors in series. More effective possible approaches need to be developed in the future.

Author contributions

L. W. designed the concept and provided revision suggestions for the manuscript. Y. Z. performed the writing of the manuscript. Q. P., M. Z., J. Z. and J. L. discussed the organization and improved the manuscript.

Conflicts of interest

The authors declare no competing financial interests.

Data availability

No primary research results, software or code have been included and no new data were generated or analysed as part of this review.

Acknowledgements

This work was supported by National Key R&D Program of China (2021YFC2103500), National Natural Science Foundation of China (22472056), the Science and Technology Commission of Shanghai Municipality (24ZR1491000), and Fundamental Research Funds for the Central Universities.

References

1 J. Strandsbjerg Tristan Pedersen, F. Duarte Santos, D. Van Vuuren, J. Gupta, R. Encarnação Coelho, B. A. Aparício and R. Swart, *Glob. Environ. Change*, 2021, **66**, 102199.
2 International Energy Agency, *Tracking Clean Energy Progress 2017*, IEA Publications, 2017.
3 J. M. Turner, *Science*, 2022, **376**, 1361.
4 L. Georgeson, M. Maslin and M. Poessinouw, *Nature*, 2016, **538**, 27–29.
5 S. Park, K. Choi, C. Lee, S. Kim, Y. Yoo and D. Chang, *Int. J. Hydrogen Energy*, 2021, **46**, 21303–21317.
6 C. Hepburn, E. Adlen, J. Beddington, E. A. Carter, S. Fuss, N. Mac Dowell, J. C. Minx, P. Smith and C. K. Williams, *Nature*, 2019, **575**, 87–97.
7 W. L. Becker, M. Penev and R. J. Braun, *J. Energy Resour. Technol.*, 2019, **141**, 021901.
8 F. Salomone, E. Giglio, D. Ferrero, M. Santarelli, R. Pirone and S. Bensaid, *Chem. Eng. J.*, 2019, **377**, 120233.
9 A. Al-Mamoori, A. Krishnamurthy, A. A. Rownaghi and F. Rezaei, *Energ. Tech.*, 2017, **5**, 834–849.
10 Y. Jiang, P. Tan, S. Qi, X. Liu, J. Yan, F. Fan and L. Sun, *Angew. Chem., Int. Ed.*, 2019, **58**, 6600–6604.
11 P. Tan, Y. Jiang, Q. Wu, C. Gu, S. Qi, Q. Zhang, X. Liu and L. Sun, *Chin. J. Chem. Eng.*, 2022, **42**, 104–111.
12 S. A. Goetz, D. T. Nguyen and A. P. Esser-Kahn, *Carbon*, 2016, **105**, 126–135.
13 C. Italiano, J. Llorca, L. Pino, M. Ferraro, V. Antonucci and A. Vita, *Appl. Catal., B*, 2020, **264**, 118494.
14 J. Zhao, P. Zhang, T. Yuan, D. Cheng, S. Zhen, H. Gao, T. Wang, Z.-J. Zhao and J. Gong, *J. Am. Chem. Soc.*, 2023, **145**, 6622–6627.
15 M. Cabrero-Antonino, A. Melillo, E. Montero-Lanzuela, M. Álvaro, B. Ferrer, I. Vayá, H. G. Baldoví and S. Navalón, *Chem. Eng. J.*, 2023, **468**, 143553.
16 Y. Liu, J. Shang and T. Zhu, *Appl. Surf. Sci.*, 2023, **639**, 158196.
17 Y. Tang, T. Zhao, H. Han, Z. Yang, J. Liu, X. Wen and F. Wang, *Adv. Sci.*, 2023, 2300122.
18 F. O. Ochedi, D. Liu, J. Yu, A. Hussain and Y. Liu, *Environ. Chem. Lett.*, 2021, **19**, 941–967.
19 H. Jiang, L. Wang, H. Kaneko, R. Gu, G. Su, L. Li, J. Zhang, H. Song, F. Zhu, A. Yamaguchi, J. Xu, F. Liu, M. Miyauchi, W. Ding and M. Zhong, *Nat. Catal.*, 2023, **6**, 519–530.
20 F. Fresno, A. Iglesias-Juez and J. M. Coronado, *Top. Curr. Chem. Z*, 2023, **381**, 21.
21 T. Zhao, Z. Yang, Y. Tang, J. Liu and F. Wang, *Energy Fuels*, 2022, **36**, 6711–6735.
22 A. V. Puga, *Top. Catal.*, 2016, **59**, 1268–1278.

23 X. Ding, W. Liu, J. Zhao, L. Wang and Z. Zou, *Adv. Mater.*, 2024, 2312093.
24 C. Wang, H. Ma, Y. Tian, A. Jiao, M. Zhang, L. Zheng, S. Li and M. Chen, *Chem. Eng. J.*, 2022, **446**, 136977.
25 L. Sun, Z. Li, R. Su, Y. Wang, Z. Li, B. Du, Y. Sun, P. Guan, F. Besenbacher and M. Yu, *Angew. Chem., Int. Ed.*, 2018, **57**, 10666–10671.
26 Y. Cai, W. Si, W. Huang, P. Chen, J. Shao and X. Dong, *Small*, 2018, **14**, 1704247.
27 Y. Zhang, S. He, W. Guo, Y. Hu, J. Huang, J. R. Mulcahy and W. D. Wei, *Chem. Rev.*, 2018, **118**, 2927–2954.
28 X. Cui, Q. Ruan, X. Zhuo, X. Xia, J. Hu, R. Fu, Y. Li, J. Wang and H. Xu, *Chem. Rev.*, 2023, **123**, 6891–6952.
29 M. Rycenga, C. M. Cobley, J. Zeng, W. Li, C. H. Moran, Q. Zhang, D. Qin and Y. Xia, *Chem. Rev.*, 2011, **111**, 3669–3712.
30 C. He, S. Wu, L. Wang and J. Zhang, *J. Photochem. Photobiol., C*, 2022, **51**, 100468.
31 U. Aslam, V. G. Rao, S. Chavez and S. Linic, *Nat. Catal.*, 2018, **1**, 656–665.
32 W. Gao, Y. Li, D. Xiao and D. Ma, *J. Energy Chem.*, 2023, **83**, 62–78.
33 F. Zarei and P. Keshavarz, *Sep. Purif. Technol.*, 2023, **323**, 124438.
34 H. Li, M. R. Hill, C. Doblin, S. Lim, A. J. Hill and P. Falcaro, *Adv. Funct. Mater.*, 2016, **26**, 4815–4821.
35 M. Li, J.-X. Xie, P. Tan, J. Liu, C. Gu, X.-Q. Liu and L.-B. Sun, *Sep. Purif. Technol.*, 2023, **318**, 123968.
36 O. Cheung, M. Åhlén, R. Chang and M. Strømme, Visible light-triggered desorption of CO_2 in green coordination polymers, *ChemRxiv*, 2023, preprint, DOI: **10.26434/chemrxiv-2023-n0lnl**.
37 D. Wang, S. Liao, S. Zhang and Y. Wang, *ChemSusChem*, 2017, **10**, 2573–2577.
38 Z. Wu, X.-H. Du, Q.-F. Zhang, M. Strømme and C. Xu, *Nano Res.*, 2023, **16**, 10617–10625.
39 W. Lu, X. Shi, H. Zhou, W. Luo, L. Wang and H. He, *Chem. Eng. J.*, 2022, **449**, 137885.
40 Y. Li, Y. Shi, H. Wang, T. Liu, X. Zheng, S. Gao and J. Lu, *Carbon Energy*, 2023, **5**, e331.
41 J. Gao, Z. Zhao, B. Wu and Y. Zhao, *Chem. Eng. J.*, 2021, **418**, 129382.
42 J. Gao, X. Song, J. Yan, J. Yuan, L. Cao, G. Deng and Z. Wang, *Chem. Eng. J.*, 2023, **455**, 140621.
43 Y. Huang, B. Zhang, K. Chen, A. Xia, X. Zhu, X. Zhu and Q. Liao, *Environ. Res.*, 2023, **216**, 114645.
44 Z. Yang, X. Liu, X. Wang, P. Wang, S. Ruan, A. Xie, Y. Shen and M. Zhu, *Chem. Eng. J.*, 2020, **387**, 124113.
45 W. Jung and J. Lee, *Energy*, 2022, **238**, 121864.
46 H. Li, K. Wang, Y. Sun, C. T. Lollar, J. Li and H.-C. Zhou, *Mater. Today*, 2018, **21**, 108–121.
47 R. E. Siegel, S. Pattanayak and L. A. Berben, *ACS Catal.*, 2023, **13**, 766–784.
48 X. Zhu, W. Xie, J. Wu, Y. Miao, C. Xiang, C. Chen, B. Ge, Z. Gan, F. Yang, M. Zhang, D. O'Hare, J. Li, T. Ge and R. Wang, *Chem. Soc. Rev.*, 2022, **51**, 6574–6651.
49 J. Schneider, H. Jia, J. T. Muckerman and E. Fujita, *Chem. Soc. Rev.*, 2012, **41**, 2036–2051.
50 C. Fukuhara, K. Hayakawa, Y. Suzuki, W. Kawasaki and R. Watanabe, *Appl. Catal., A*, 2017, **532**, 12–18.
51 F. Zhang, Y.-H. Li, M.-Y. Qi, Y. M. A. Yamada, M. Anpo, Z.-R. Tang and Y.-J. Xu, *Chem Catal.*, 2021, **1**, 272–297.
52 Z. Li, C. Mao, Q. Pei, P. N. Duchesne, T. He, M. Xia, J. Wang, L. Wang, R. Song, F. M. Ali, D. M. Meira, Q. Ge, K. K. Ghuman, L. He, X. Zhang and G. A. Ozin, *Nat. Commun.*, 2022, **13**, 7205.
53 Y. Wang, E. Chen and J. Tang, *ACS Catal.*, 2022, **12**, 7300–7316.
54 M. Ghoussoub, M. Xia, P. N. Duchesne, D. Segal and G. Ozin, *Energy Environ. Sci.*, 2019, **12**, 1122–1142.
55 S. Luo, X. Ren, H. Lin, H. Song and J. Ye, *Chem. Sci.*, 2021, **12**, 5701–5719.
56 F. Sastre, C. Versluis, N. Meulendijks, J. Rodríguez-Fernández, J. Sweelssen, K. Elen, M. K. Van Bael, T. Den Hartog, M. A. Verheijen and P. Buskens, *ACS Omega*, 2019, **4**, 7369–7377.
57 R. Grote, R. Habets, J. Rohlfs, F. Sastre, N. Meulendijks, M. Xu, M. A. Verheijen, K. Elen, A. Hardy, M. K. Van Bael, T. Den Hartog and P. Buskens, *ChemCatChem*, 2020, **12**, 5618–5622.
58 J. Rohlfs, K. W. Bossers, N. Meulendijks, F. Valega Mackenzie, M. Xu, M. A. Verheijen, P. Buskens and F. Sastre, *Catalysts*, 2022, **12**, 126.
59 M. Novoa-Cid and H. G. Baldovi, *Nanomaterials*, 2020, **10**, 2212.
60 T. Dong, X. Liu, Z. Tang, H. Yuan, D. Jiang, Y. Wang, Z. Liu, X. Zhang, S. Huang, H. Liu, L. Zhao and W. Zhou, *Appl. Catal., B*, 2023, **326**, 122176.
61 Y. Chen, Y. Zhang, G. Fan, L. Song, G. Jia, H. Huang, S. Ouyang, J. Ye, Z. Li and Z. Zou, *Joule*, 2021, **5**, 3235–3251.
62 J. Tian, R. Han, Q. Guo, Z. Zhao and N. Sha, *Catalysts*, 2022, **12**, 612.
63 S. Kim, M. Kim, S.-H. Hwang and S. K. Lim, *Appl. Catal., B*, 2012, **123–124**, 391–397.
64 K. Kato, Y. Xin, J. Hong, K. Katsumata and T. Shirai, *Adv. Powder Technol.*, 2020, **31**, 1777–1783.
65 S. Wang, M. Cabrero-Antonino, S. Navalón, C. Cao, A. Tissot, I. Dovgaliuk, J. Marrot, C. Martineau-Corcos, L. Yu, H. Wang, W. Shepard, H. García and C. Serre, *Chem*, 2020, **6**, 3409–3427.
66 M. Cabrero-Antonino, B. Ferrer, H. G. Baldoví and S. Navalón, *Chem. Eng. J.*, 2022, **445**, 136426.
67 C. Han, X. Zhang, S. Huang, Y. Hu, Z. Yang, T. Li, Q. Li and J. Qian, *Adv. Sci.*, 2023, **10**, 2300797.
68 Y. Tang, Z. Yang, C. Guo, H. Han, Y. Jiang, Z. Wang, J. Liu, L. Wu and F. Wang, *J. Mater. Chem. A*, 2022, **10**, 12157–12167.
69 D. Mateo, D. De Masi, J. Albero, L. Lacroix, P. Fazzini, B. Chaudret and H. García, *Chem.–Eur. J.*, 2018, **24**, 18436–18443.
70 X. Zhang, H. Liu, Y. Wang, S. Yang, Q. Chen, Z. Zhao, Y. Yang, Q. Kuang and Z. Xie, *Chem. Eng. J.*, 2022, **443**, 136482.
71 X. Zhang, X. Li, D. Zhang, N. Q. Su, W. Yang, H. O. Everitt and J. Liu, *Nat. Commun.*, 2017, **8**, 14542.

72 X. Zhang, X. Li, M. E. Reish, D. Zhang, N. Q. Su, Y. Gutiérrez, F. Moreno, W. Yang, H. O. Everitt and J. Liu, *Nano Lett.*, 2018, **18**, 1714–1723.
73 S. Jantarang, E. C. Lovell, T. H. Tan, J. Scott and R. Amal, *Prog. Nat. Sci.*, 2018, **28**, 168–177.
74 Z. Wu, C. Li, Z. Li, K. Feng, M. Cai, D. Zhang, S. Wang, M. Chu, C. Zhang, J. Shen, Z. Huang, Y. Xiao, G. A. Ozin, X. Zhang and L. He, *ACS Nano*, 2021, **15**, 5696–5705.
75 D. Mateo, N. Morlanes, P. Maity, G. Shterk, O. F. Mohammed and J. Gascon, *Adv. Funct. Mater.*, 2021, **31**, 2008244.
76 T. H. Tan, B. Xie, Y. H. Ng, S. F. B. Abdullah, H. Y. M. Tang, N. Bedford, R. A. Taylor, K.-F. Aguey-Zinsou, R. Amal and J. Scott, *Nat. Catal.*, 2020, **3**, 1034–1043.
77 T. M. Steeves and A. P. Esser-Kahn, *RSC Adv.*, 2021, **11**, 8394–8397.
78 X. Zhu, H. Zong, C. J. V. Pérez, H. Miao, W. Sun, Z. Yuan, S. Wang, G. Zeng, H. Xu, Z. Jiang and G. A. Ozin, *Angew. Chem., Int. Ed.*, 2023, **62**, e202218694.
79 E. T. Kho, S. Jantarang, Z. Zheng, J. Scott and R. Amal, *Engineering*, 2017, **3**, 393–401.
80 P. Li, S. Zhang, Z. Xiao, H. Zhang, F. Ye, J. Gu, J. Wang, G. Li and D. Wang, *Fuel*, 2024, **357**, 129817.
81 D. Xu, Z. Li, L. Li and J. Wang, *Adv. Funct. Mater.*, 2020, **30**, 2000712.
82 Z.-H. He, Z.-H. Li, Z.-Y. Wang, K. Wang, Y.-C. Sun, S.-W. Wang, W.-T. Wang, Y. Yang and Z.-T. Liu, *Green Chem.*, 2021, **23**, 5775–5785.
83 C. Singhvi, G. Sharma, R. Verma, V. K. Paidi, P. Glatzel, P. Paciok, V. B. Patel, O. Mohan and V. Polshettiwar, *Proc. Natl. Acad. Sci. U. S. A.*, 2025, **122**, e2411406122.
84 X. Yu, X. Ding, Y. Yao, W. Gao, C. Wang, C. Wu, C. Wu, B. Wang, L. Wang and Z. Zou, *Adv. Mater.*, 2024, 2312942.
85 F. Yang, X. Liu, C. Xing, Z. Chen, L. Zhao, X. Liu, W. Gao, L. Zhu, H. Liu and W. Zhou, *Adv. Sci.*, 2024, 2406828.
86 Y. Li, J. Hao, H. Song, F. Zhang, X. Bai, X. Meng, H. Zhang, S. Wang, Y. Hu and J. Ye, *Nat. Commun.*, 2019, **10**, 2359.
87 S. Sun, H. Sun, P. T. Williams and C. Wu, *Sustainable Energy Fuels*, 2021, **5**, 4546–4559.
88 R. Rajamathi, Bhojaraj and C. Nethravathi, *ACS Appl. Nano Mater.*, 2021, **4**, 10969–10975.
89 Z. Zhou, N. Sun, B. Wang, Z. Han, S. Cao, D. Hu, T. Zhu, Q. Shen and W. Wei, *ChemSusChem*, 2020, **13**, 360–368.
90 P. Huang, J. Chu, J. Fu, J. Yu, S. Li, Y. Guo, C. Zhao and J. Liu, *Chem. Eng. J.*, 2023, **467**, 143431.
91 Y. Xia, Z. Tian, T. Heil, A. Meng, B. Cheng, S. Cao, J. Yu and M. Antonietti, *Joule*, 2019, **3**, 2792–2805.
92 Y. Xia, B. Cheng, J. Fan, J. Yu and G. Liu, *Sci. China Mater.*, 2020, **63**, 552–565.
93 Z. Wang, Z. Yang, Z. C. Kadirova, M. Guo, R. Fang, J. He, Y. Yan and J. Ran, *Coord. Chem. Rev.*, 2022, **473**, 214794.
94 G. Ding, Z. Wang, J. Zhang, P. Wang, L. Chen and G. Liao, *EcoEnergy*, 2024, **2**, 22–44.
95 Y. Horiuchi, K. Miyazaki, M. Tachibana, K. Nishigaki and M. Matsuoka, *Res. Chem. Intermed.*, 2023, **49**, 1131–1146.
96 Z. Xie, W. Cheng, H. Luo, Y. Lei and W. Shi, *Adv. Energy Mater.*, 2025, 2501840.
97 D. Jiang, Y. Zhou, Q. Zhang, Q. Song, C. Zhou, X. Shi and D. Li, *ACS Appl. Mater. Interfaces*, 2021, **13**, 46772–46782.
98 Y. Wu, M. Wu, J. Zhu, X. Zhang, J. Li, K. Zheng, J. Hu, C. Liu, Y. Pan, J. Zhu, Y. Sun and Y. Xie, *Sci. China Chem.*, 2023, **66**, 1997–2003.
99 Y. Ren, Y. Fu, N. Li, C. You, J. Huang, K. Huang, Z. Sun, J. Zhou, Y. Si, Y. Zhu, W. Chen, L. Duan and M. Liu, *Nat. Commun.*, 2024, **15**, 4675.
100 Y. Liao, S. Cao, Y. Yuan, Q. Gu, Z. Zhang and C. Xue, *Chem.–Eur. J.*, 2014, **20**, 10220–10222.
101 Y. Liao, Z. Hu, Q. Gu and C. Xue, *Molecules*, 2015, **20**, 18847–18855.
102 X. Ding, X. Liu, J. Cheng, L. Kong and Y. Guo, *Catal. Sci. Technol.*, 2022, **12**, 4740–4752.
103 K. Du, J. Guo, C. Song, X. Liu, M. Chen, D. Yuan, R. Ye, X. San, Y. Li and J. Ye, *Energy Environ. Sci.*, 2025, **18**, 1255–1261.
104 J. Y. Y. Loh, A. Mohan, A. G. Flood, G. A. Ozin and N. P. Kherani, *Nat. Commun.*, 2021, **12**, 402.
105 L. Hurtado, A. Mohan, U. Ulmer, R. Natividad, A. A. Tountas, W. Sun, L. Wang, B. Kim, M. M. Sain and G. A. Ozin, *Chem. Eng. J.*, 2022, **435**, 134864.
106 S. Bhatta, D. Nagassou, S. Mohsenian and J. P. Trelles, *Sol. Energy*, 2019, **178**, 201–214.
107 X. Liu, C. Xing, F. Yang, Z. Liu, Y. Wang, T. Dong, L. Zhao, H. Liu and W. Zhou, *Adv. Energy Mater.*, 2022, **12**, 2201009.
108 Y. Li, J. Hao, H. Song, F. Zhang, X. Bai, X. Meng, H. Zhang, S. Wang, Y. Hu and J. Ye, *Nat. Commun.*, 2019, **10**, 2359.
109 X. Kang, D. Yuan, Z. Yi, C. Yu, X. Yuan, B. Liang, X. San, L. Gao, S. Wang and Y. Li, *Catal. Sci. Technol.*, 2022, **12**, 5559–5564.
110 S. Zoller, E. Koepf, D. Nizamian, M. Stephan, A. Patané, P. Haueter, M. Romero, J. González-Aguilar, D. Lieftink, E. De Wit, S. Brendelberger, A. Sizmann and A. Steinfeld, *Joule*, 2022, **6**, 1606–1616.
111 R. Schäppi, D. Rutz, F. Dähler, A. Muroyama, P. Haueter, J. Lilliestam, A. Patt, P. Furler and A. Steinfeld, *Nature*, 2022, **601**, 63–68.
112 M. Jouny, W. Luc and F. Jiao, *Ind. Eng. Chem. Res.*, 2018, **57**, 2165–2177.
113 X. Ding, Z. Zhang, J. Sun, J. Y. Y. Loh, D. Ji, J. Lu, C. Liu, L. Zhao, W. Liu, J. Zhao, S. Tang, M. Safari, H. Cai, W. Tu, N. P. Kherani, Z. Hu, G. A. Ozin, Z. Zou and L. Wang, *Joule*, 2023, **7**, 2318–2334.
114 S. Yun, S.-Y. Oh and J.-K. Kim, *Appl. Energy*, 2020, **268**, 114933.
115 C. Choe, B. Lee, A. Kim, S. Cheon and H. Lim, *Green Chem.*, 2021, **23**, 9502–9514.
116 C. Vogt, M. Monai, G. J. Kramer and B. M. Weckhuysen, *Nat. Catal.*, 2019, **2**, 188–197.

